Journal of
Marine Science and Engineering

Article

Hydroelastic Response to Oblique Wave Incidence on a Floating Plate with a Submerged Perforated Base

Sarat Chandra Mohapatra * and C. Guedes Soares

Centre for Marine Technology and Ocean Engineering (CENTEC), Instituto Superior Técnico, Universidade de Lisboa, Av. Rovisco Pais, 1049-001 Lisboa, Portugal
* Correspondence: sarat.mohapatra@centec.tecnico.ulisboa.pt

Abstract: A hydroelastic model is developed of a floating flexible structure in the presence of a submerged perforated base connected with mooring lines under oblique wave action. Using the velocity decomposition method, the analytical solution of the referred model is obtained in finite water depth. The convergence of the analytical solution for different oblique wave incidences is examined, and the present results of deflection amplitude are compared with experimental datasets and the numerical results available in the literature. The effects of oblique wave incidence, along with various design parameters on the reflection, transmission, and dissipation coefficients, as well as structural displacements, are analysed through hydroelastic analysis. Further, the effect of oblique incidence angle on the free oscillation hydroelastic waves in two wave modes is investigated by deriving the free motion velocity potential in a wave basin.

Keywords: horizontal flexible plate; oblique wave incidence; hydroelasticity; plate displacement; free oscillations; wave basin

check for updates

Citation: Mohapatra, S.C.; Soares, C.G. Hydroelastic Response to Oblique Wave Incidence on a Floating Plate with a Submerged Perforated Base. *J. Mar. Sci. Eng.* **2022**, *10*, 1205. https://doi.org/10.3390/jmse10091205

Academic Editor: Eva Loukogeorgaki

Received: 15 July 2022
Accepted: 25 August 2022
Published: 28 August 2022

1. Introduction

Due to the rise in marine and human activities in offshore and coastal regions, there is considerable significance in the application of horizontal flexible floating and or submerged structures as breakwaters for protecting coastal infrastructures and offshore platforms. To meet the increasing demand for coastal protection and utilization of ocean space, there is a need to develop and analyse multi-use flexible structure systems that could be applied as floating breakwaters or land-filled artificial islands. Therefore, for practical engineering design, it is necessary to examine the hydrodynamic performance of flexible structures through hydroelastic analysis (see [1–3]). Hence, the interest in designing or modelling horizontal floating and submerged flexible porous structures have increased to investigate their effectiveness via hydroelastic analysis.

These types of horizontal structures are unique in nature, primarily because of their flexibility; displacement; and associated hydroelastic response, analysis, and design when compared with fixed structures. Constructions of these structures are cost-effective when the water depth is large as they are easy and fast to construct and can be removed or expanded with ease. These structures are protected from seismic shocks because the energy can be dissipated into the infinite ocean, and they do not damage the marine eco-system or obstruct the ocean current and are thus environmentally friendly. On the other hand, the effectiveness of these flexible porous structures is due to the fact that they are able to reflect, absorb, and dissipate wave energy. Moreover, the use of flexible porous structures has great advantages compared to rigid impermeable structures because the structural porosity helps in dissipating a large amount of wave energy, and the flexibility of the structure provide the additional feature of wave attenuation through structural displacement [4].

Commonly, the potential theory is used for the analysis of the linearized hydroelastic problem under the assumption of small wave amplitude. The classical thin-plate theory is frequently employed to analyse the dynamic response of floating structures (see [5,6]). On the other hand, the dynamic response of offshore platforms and wave loads on floating bridges were studied in [7]. The hydroelasticity modelling challenges associated with problems in various areas of engineering applications in offshore and arctic regions are reviewed in [8]. The mathematical theory and methods of hydroelasticity for solving problems associated with wave interaction with floating flexible structures are viewed as the major challenges to adequate and successful treatment of such complex models in the application of technology development.

In past studies, there have been several types of numerical methods successfully used in marine engineering to investigate the hydrodynamic effect of fluid-structure interaction problems. For example, the Finite Volume Method in [9], the Arbitrary Lagrangian-Eulerian Method in [10], particle-based methods, such as the Smoothed Particle Hydrodynamics in [11], coupled methods, such as coupled SPH-DEM in [12], coupled SPH-FEM in [13], and ANSYS® AQWA (henceforth called only AQWA for simplicity), which is a BEM code [14]. On the other hand, the hydroelastic analysis of various geometries of very large floating structures (VLFS) was studied based on different numerical methodologies. For instance, the hydroelastic analysis of VLFS by attaching an annular plate below VLFS using the Rayleigh–Ritz technique was investigated in [15]. The hydroelastic response of VLFS using vertical elastic mooring lines was studied in [16] based on the hybrid finite element–boundary element method. Further, a Finite Element-Multi-Domain Boundary Element method was presented for the hydroelastic analysis of VLFSs with perforated plates attached at the fore or aft under linear wave theory in [17]. A hydroelastic model based on the multi-mode expansion and the Finite Element Method (FEM) was developed in 2D for VLFS in [18], along with a coupled-mode model in 3D over the variable bottom (see [19]). Based on the BIEM approach, the effect of mooring lines on a floating flexible plate was analysed in [20]. The hydroelastic responses of a submerged horizontal porous plate attached at the front of a VLFS of rectangular type were analysed in [21] based on the matched eigenfunction expansion method (MEFEM).

Another interesting aspect of this class of problem is the analysis of wave loads, displacements, and the moment of the structure under the action of waves. The wave-induced loads on the deck and beam elements were measured based on physical model tests of exposed piers/jetties/bridges in [22]. A finite-element analysis (FEA) code, LS-DYNA, is used to perform the CFD analysis and compute the wave loading on coastal bridges in [23]. A large-scale hydrodynamic experiment of tsunami wave interaction with an I-girder bridge with cross frames was presented to analyse the impact of tsunamis on bridge inundation mechanisms as well as the associated connection forces between the super- and sub-structures of these bridges [24]. The significant effect of the trapped air on the pressures, total forces, and the response of coastal bridges were studied in [25] based on experiments. Further, the forces on a bridge superstructure in the horizontal and vertical directions based on experimental and numerical hydrodynamic models were investigated to determine the effect of variations in bridge elevation and wave height on the magnitude of the horizontal and vertical forces and overturning moment [26].

There has been considerable progress in understanding the behaviour of submerged horizontal porous structures and their effect on floating flexible structures based on MEFEM. The interaction of oblique monochromatic waves with a submerged horizontal porous plate in the framework of two-dimensional potential flow was inspected in [27] based on MEFEM, and reflection and transmission coefficients were further studied using the Boundary Element Method (BEM) in [28]. In [29], a time-domain hybrid FEM-BEM was presented to investigate the interaction between oblique irregular waves and a very large floating structure (VLFS) edged with dual inclined perforated plates.

The hydroelastic response of a mat-like rectangular VLFS with dual horizontal inclined porous anti-motion plates using BEM was investigated in [30]. The hydroelastic problem of a pontoon-type VLFS connected with porous plates and non-porous plates was studied in [31], both numerically and experimentally. Under velocity decomposition, an analytical model of surface gravity waves with a submerged flexible membrane in the presence of a floating elastic plate connected with mooring lines was presented in [32]. Further, a 3D analytical hydroelastic model of a floating and a submerged flexible plate was developed (see [33]) to study the effect of mooring lines and modes of oscillation on a floating elastic plate in the presence of a submerged fixed membrane in the water of finite depth (FD) under ocean wave action.

Therefore, here, a mathematical model of a floating horizontal flexible structure in the presence of a submerged perforated structure connected with mooring lines of finite dimensions under oblique waves is developed to analyse the effect of oblique incident angle in FD.

The new contributions of the present physical model compared with [34] are the reduced wave equation, boundary conditions, and solutions, along with the comparison of results of deflection amplitudes with existing published experimental datasets and the numerical BEM-FEM model. Further, the effect of oblique wave incidence angle along with different design parameters on the moored floating flexible structure with a moored submerged porous structure is investigated by analysing the reflection, transmission, and dissipation coefficients as well as plate displacements in different cases via hydroelastic analysis. In addition, the effect of oblique incidence angle on the free oscillation hydroelastic waves in a wave tank is investigated in two wave modes.

2. Model Definition

A similar model in two dimensions was analysed in [34]. Here, the effect of oblique incident angle on the reflection, transmission, and dissipation coefficients and plate displacements are analysed in three dimensions, presenting significant contributions towards formulation and solutions, and the results are discussions.

The model is defined under the hypothesis of linear wave theory and the Cartesian variables (x, y, z), where the $x - z$ plane is considered as the still position of the water surface and the y-axis is pointing positively downward. A horizontal floating and submerged porous plate with a length of $2L$ occupies $-L < x < L$ $0 < z < \infty$ and is placed at $y = 0$ (floating plate), and a porous plate is situated at $y = d$ that also occupies $-L < x < L$ and $0 < z < \infty$ with the bottom bed $y = h$ FD. For practical interest, both plates are connected with mooring lines with stiffnesses q_{fj} and q_{sj} at $x = \pm L$ for $j = 1, 2$, and they are extended along the z-direction at $0 < z < \infty$. Structural dimensions and problem definitions are presented in Figure 1.

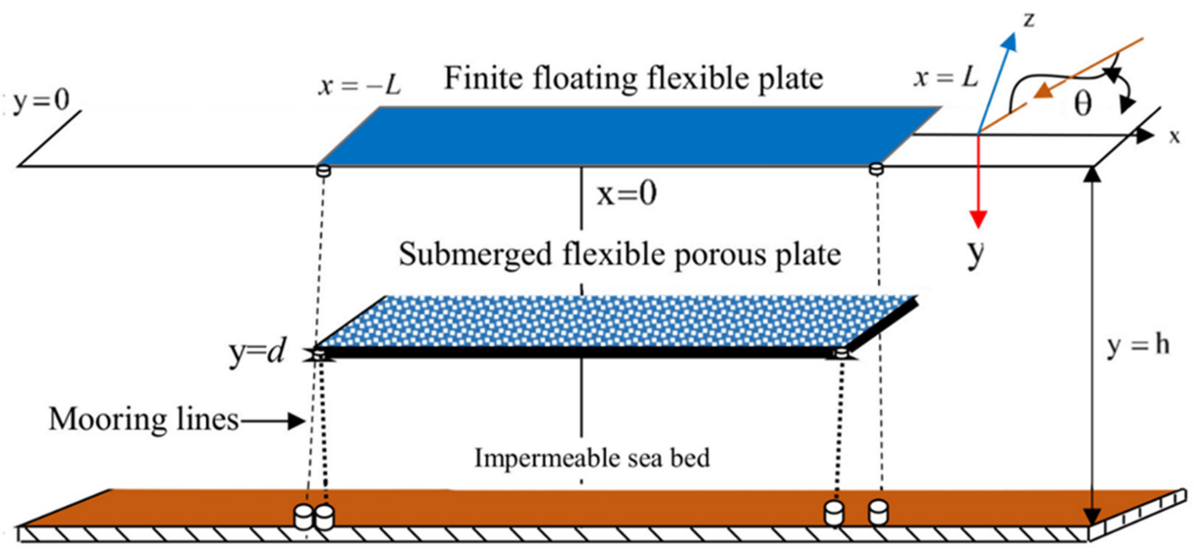

Figure 1. Schematic diagram.

Therefore, the entire fluid region is bifurcated as:

$$\text{Fluid domain} = \begin{cases} -\infty < x < -L, L < x < \infty, y \in (0,h),\ 0 < z < \infty \text{ (Open water region)}, \\ -L < x < L, y \in (0,d) \cup (d,h),\ 0 < z < \infty \text{ (Plate covered region)}. \end{cases} \tag{1}$$

It is assumed that a progressive wave is obliquely incident with an angle, θ, on the floating and submerged porous plate along the x-axis. Further, the fluid is modelled as inviscid and incompressible, and the motion is irrotational.

It should be mentioned that there are many areas in applied mathematics and engineering, especially in fluid flows and elastic plate/membranes, which leads to the solution of the Laplace equation in two/three dimensions. The appropriate choice of boundary conditions is of paramount importance in the selection of appropriate mathematical tools to solve the problem of interest. Often, the three-dimensional Laplace equation is further simplified to $\Phi(x,y,z;t) = \mathrm{Re}\left\{\phi(x,y)e^{i(\gamma z-\omega t)}\right\}$, which reduces the three-dimensional Laplace equation to a two-dimensional elliptic PDE so-called reduced wave equation. Moreover, the z-component is absorbed by the term γ, which is associated with the z-component of the wavenumber β_0, associated with the incident waves in the open water region.

Therefore, the linear wave theory yields to the velocity potential, $\Phi(x,y,z;t) = \mathrm{Re}\left\{\phi(x,y)e^{i(\gamma z-\omega t)}\right\}$, for a fluid motion that is simple and harmonic in time, with an angular frequency, ω, where $i = \sqrt{-1}$, $\gamma = \beta_0 \sin\theta$ is the z-component of the wavenumber β_0 associated with the incident waves in open water regions, and $\phi(x,y)$ refers to the spatial velocity potential and satisfies the reduced wave equation:

$$(\nabla^2_{xy} - \gamma^2)\phi = 0, \text{ in the fluid domain} \tag{2}$$

where $\nabla^2_{xy} = \partial^2/\partial x^2 + \partial^2/\partial y^2$.

The linearized free surface at $y = 0$ is derived by combining the linearized kinematic and dynamic conditions as:

$$\phi_y + \tau\phi = 0, -\infty < x < -L, L < x < \infty \text{ with } \tau = \omega^2/g \tag{3}$$

The usual non-flow condition in water of FD at $y = h$ can be read as:

$$\phi_y = 0, -\infty < x < \infty \tag{4}$$

Now, the boundary conditions on $y = 0$ give (as in [34]):

$$\kappa_1 \frac{\partial^5\phi_1}{\partial y^5} - \varepsilon_1 \frac{\partial^3\phi_1}{\partial y^3} + \frac{\partial\phi_1}{\partial y} + \tau\phi_1 = 0 \text{ on } y = 0 \text{ for } -L < x < L, z < \infty \tag{5}$$

The boundary condition on $y = d$ are given by:

$$\phi_{2y} = \phi_{1y} = -i\omega w_2 + i\sigma(\phi_2 - \phi_1) \text{ on } y = d \tag{6}$$

$$\begin{gathered}\left(\kappa_2 \frac{\partial^5\phi_2}{\partial y^5} - \varepsilon_2 \frac{\partial^3\phi_2}{\partial y^3} - m_{p2}\frac{\partial\phi_2}{\partial y} + \tau\phi_2\right) + i\sigma\left(\kappa_2 \frac{\partial^4}{\partial y^4} - \varepsilon_2 \frac{\partial^2}{\partial y^2} - m_{p2}\frac{\partial}{\partial y}\right)(\phi_2 - \phi_1) - \tau\phi_1 = 0, \\ y = d, -L < x < L, z < \infty\end{gathered} \tag{7}$$

where $\kappa_j = E_j I_j/(\rho g - m_{pj}\omega^2)$, $\varepsilon_j = N_j/(\rho g - m_{pj}\omega^2)$, and $\tau = \rho\omega^2/(\rho g - m_{pj}\omega^2)$. Further, $m_{p_j} = \rho_{pj} a_j$ is the mass per unit length and a_j is the thickness of the plate. In addition, E_j, $I_j = a_j^3/12(1-\upsilon^2)$, and υ is the Poisson's ratio of each plate. In addition, N_j is the uniform compressive force ($N_{jx} = N_{jz} = N_j$, $j = 1,2$ where N_1 and N_2 are the uniform compressive forces acting on the plates). Further, σ is the porous-effect parameter of the submerged flexible porous plate where $\sigma = \sigma_r + i\sigma_i$ is the complex porous effect parameter, as in [35], where σ_r is the resistance force coefficient and σ_i is the inertial force coefficient. The subscripts t and y refer to the partial derivatives w. r. t. t and y, respectively. Further, $w_2(x,z;t)$ denotes the submerged porous plate deflection. ϕ_1 and ϕ_2 denote the velocity potentials for the region $-L < x < L$, $0 < y < d$, $0 < z < \infty$ and $-L < x < L$, $d < y < h$, $0 < z < \infty$, respectively. Further, w_2, defined in Equation (6), is the deflection of the submerged porous plate and is assumed by the following form:

$w_2(x,z;t) = \mathrm{Re}\left\{w_{20}(x)e^{i(\gamma z-\omega t)}\right\}$.

The moored edge conditions at $x = \pm L,\ y = 0$ of the floating flexible plate give:

$$E_1 I_1\left(\partial_{xx} - v\gamma^2\right)\phi_y = 0 \tag{8}$$

$$\left[E_1 I_1\left(\partial_{xx} - (2-v)\gamma^2\right)\partial_x + N_1\partial_x\right]\phi_y = q_{fj}\phi_y \tag{9}$$

Additionally, the moored edge conditions at $x = \pm L,\ y = d$ provide:

$$E_2 I_2(\partial_{xx} - v\gamma^2)\phi_y = 0 \tag{10}$$

$$\left[E_2 I_2\left(\partial_{xx} - (2-v)\gamma^2\right)\partial_x + N_2\partial_x\right]\phi_y = q_{sj}\phi_y \tag{11}$$

Further, the following continuity conditions at $(0,\ r)$ with $r = 0, d$ are necessary to solve this referred physical problem:

$$\phi_y\big|_{(0^+,r)} = \phi_y\big|_{(0^-,r)}, \phi_{xy}\big|_{(0^+,r)} = \phi_{xy}\big|_{(0^-,r)} \tag{12}$$

$$\left.\begin{array}{l} E_j I_j(\partial_{xx} + v\partial_{zz})\phi_y\Big|_{(0^+,r)} = E_j I_j(\partial_{xx} + v\partial_{zz})\phi_y\Big|_{(0^+,r)}, \\ \Big[\partial_x[E_j I_j\{\partial_{xx} + (2-v)\partial_{zz}\} + N_j]\phi_y\Big]\Big|_{(0^+,r)} = \Big[\partial_x[E_j I_j\{\partial_{xx} + (2-v)\partial_{zz}\} + N_j]\phi_y\Big]\Big|_{(0^-,r)}. \end{array}\right\} \tag{13}$$

The continuity of pressure and velocity at $x = 0^{\pm}, L^{\pm}$ give:

$$\phi(0^+,y) = \phi(0^-,y), \phi(L^+,y) = \phi(L^-,y) \tag{14}$$

$$\phi_x(0^+,y) = \phi_x(0^-,y), \phi_x(L^+,y) = \phi_x(L^-,y) \tag{15}$$

In the end, the far-field radiation condition related to the incident, reflected, ane transmitted wave amplitudes, I_0, R_0, and T_0, respectively give:

$$\phi(x,y) = \left\{\begin{array}{ll} \left(I_0 e^{-i\mu_0 x} + R_0 e^{i\mu_0 x}\right)\Omega(y) & \text{as } x \to \infty, \\ T_0 e^{-i\mu_0 x}\Omega(y) & \text{as } x \to -\infty \end{array}\right. \tag{16}$$

where $\Omega(y) = \cosh\beta_0(h-y)/\cosh\beta_0 h$ with $\mu_0^2 = \beta_0^2 - \gamma^2$ and β_0 is the real root and satisfies the gravity wave dispersion relation $\omega^2 = g\beta_0\mathrm{tanh}\beta_0 h$ in the open water region.

2.1. Solution

By considering the geometrical symmetry of the physical problem regarding x = 0, the velocity potentials associated with the physical problems are rewritten as the sum of the symmetric and antisymmetric potentials for simplification, which can be handled easily for the solution at hand. Hence, the original problem is split into two simpler problems in the semi-infinite region along the x-axis of $0 < z < \infty$. Here, to derive the system of equations, the orthogonal relation associated with the eigenfunctions in the open water region is used. Hence, it is sufficient to consider only the region $0 < x < \infty$ of $0 < z < \infty$ because the solution can be extended into the whole fluid domain using symmetric relations. Proceeding similarly as in [2], the split potentials, $\mathbb{L}(x,y)$ and $\hat{\mathbb{L}}(x,y)$, fulfil Equations (1)–(6), and can be written as:

$$\mathbb{L}(x,y) = \begin{cases} \sum_n a_n \Psi_n^S(x,y), 0 < x < L, \text{ for } n = 0, I, II, III, 1, 2, \ldots \\ I_0\Gamma_0(x,y) + \sum_n b_n \Gamma_n(x,y), L < x < \infty, \text{ for } n = 0, 1, 2, \ldots \end{cases} \tag{17}$$

$$\hat{\mathbb{L}}(x,y) = \begin{cases} \sum_n \overline{a}_n \Psi_n^S(x,y) \text{ for } 0 < x < L, \text{ for } n = 0, I, II, III, 1, 2, \ldots \\ I_0\Gamma_0(x,y) + \sum_n \overline{b}_n \Gamma_n(x,y) \text{ for } L < x < \infty, \text{ for } n = 0, 1, 2, \ldots \end{cases} \tag{18}$$

where $\Psi^S(x,y) = J_n^S(x) f_n(y)$, $J_n^S(x) = (\cosh\alpha_n x)/(\cosh\alpha_n L)$, $\Psi^A(x,y) = J_n^A(x) f_n(y)$, $J_n^A(x) = (\sinh\alpha_n x)/(\sinh\alpha_n L)$, $\Gamma_0(x,y) = e^{-i\mu_0(x-L)}\varphi_0(y)$, $\Gamma_n(x,y) = e^{i\mu_n(x-L)}\varphi_n(y)$,

$$f_n(\alpha_n, y) = \begin{cases} \frac{Q_1(\alpha_n,y)\operatorname{csch}\alpha_n d}{N_1(\alpha_n,d)}, y \in (0,d), \\ -i\{\tau + i\sigma(\kappa_2\alpha_n^4 - \varepsilon_2\alpha_n^2)\}\frac{\cosh\alpha_n(h-y)}{\cosh\alpha_n H}, d < y < h, \end{cases} \tag{19}$$

$$Q_1(\alpha_n, y) = \left\{\tau + i\sigma(\kappa_2\alpha_n^4 - \varepsilon_2\alpha_n^2)\right\}\left\{\alpha_n(\kappa_1\alpha_n^4 - \varepsilon_1\alpha_n^2 + 1)\cosh\alpha_n y - \tau\sinh\alpha_n y\right\} \tag{20}$$

where $\alpha_n^2 = \beta_n^2 - \gamma^2$ and α_ns are the zeros of the dispersion relation:

$$\begin{aligned} Z(\alpha) = {} & \tau^2(1 + \coth\alpha d\coth\alpha H) - \tau[\alpha(\kappa_1\alpha^4 - \varepsilon_1\alpha^2 + 1)\coth\alpha H \\ & + \{\alpha(\kappa_2\alpha^4 - \varepsilon_2\alpha^2) + \alpha(\kappa_1\alpha^4 - \varepsilon_1\alpha^2 + 1)\}\coth\alpha d \\ & - i\sigma(\kappa_2\alpha^4 - \varepsilon_2\alpha^2)(1 + \coth\alpha d\coth\alpha H)] + \alpha^2(\kappa_1\alpha^4 - \varepsilon_1\alpha^2 + 1)(\kappa_2\alpha^4 - \varepsilon_2\alpha^2) \\ & - i\sigma\alpha(\kappa_2\alpha^4 - \varepsilon_2\alpha^2)(\kappa_1\alpha^4 - \varepsilon_1\alpha^2 + 1)(\coth\alpha d + \coth\alpha H), \end{aligned} \tag{21}$$

where $\tau = \omega^2/g$ and $H = h - d$; if $\gamma = 0$ in Equation (16), then the truncated result will be the same as in [34]. All roots of the dispersion relation (21) are complex (for details, see [34] (below Equation (19)). It should be mentioned that, assuming the practical interest of the problem, only four roots are taken into account for the boundedness of the solution. The normalized vertical eigenfunction $\varphi_n(y)$ is obtained by replacing $\phi_n(y)$ in Equation (49) of [34].

2.2. Boundary Conditions in Connection with $\mathbb{L}(x,y)$ and $\hat{\mathbb{L}}(x,y)$

Boundary conditions (7)–(9) need to be expressed in connection with $\mathbb{L}$ and $\hat{\mathbb{L}}$ to determine the constants $a_n, b_n, \overline{a}_n,$ and $\overline{b}_n$ associated with Equations (10) and (11). Hence, conditions (8)–(11) can be reformulated as:

$$E_1 I_1\left(\partial_{xx} - \upsilon\gamma^2\right)\frac{\partial\mathbb{L}(L,0)}{\partial y} = 0 \tag{22}$$

$$\begin{gathered} \partial_x[E_1 I_1\{\partial_{xx} - (2-\upsilon)\gamma^2\} + N_1]\frac{\partial\hat{\mathbb{L}}(L,0)}{\partial y} = q_f\frac{\partial^2\hat{\mathbb{L}}(L,0)}{\partial x\partial y} \\ E_2 I_2(\partial_{xx} - \upsilon\gamma^2)\frac{\partial\mathbb{L}(L,d)}{\partial y} = 0 \end{gathered} \tag{23}$$

$$\partial_x[E_2 I_2\left\{\partial_{xx} - (2-\upsilon)\gamma^2\right\} + N_2]\frac{\partial\hat{\mathbb{L}}(L,d)}{\partial y} = q_s\frac{\partial^2\hat{\mathbb{L}}(L,d)}{\partial x\partial y} \tag{24}$$

where υ is the Poisson's ratios of floating and submerged flexible plates.

Further, the continuity conditions (12) and (13) at (*0, r*) in terms $\mathbb{L}(x,y)$ and $\hat{\mathbb{L}}(x,y)$ can be expressed as:

$$\mathbb{L}_y(0,r) = 0,\ \mathbb{L}_{xy}(0,r) = 0 \tag{25}$$

$$E_j I_j\left(\partial_{xx} - \upsilon\gamma^2\right)\hat{\mathbb{L}}_y(0,r) = 0 \tag{26}$$

$$\partial_x[E_j I_j\left\{\partial_{xx} - (2-\upsilon)\gamma^2\right\} + N_j]\hat{\mathbb{L}}_y(0,r) = 0 \tag{27}$$

The continuity conditions (14) and (15) give:

$$\mathbb{L}(x,y) = 0, \text{ at } x = L \tag{28}$$

$$\frac{\partial \hat{\mathbb{L}}(x,y)}{\partial x} = 0. \text{ at } x = L. \tag{29}$$

In the end, the condition as $x \to \infty$ satisfy:

$$\mathbb{L}(x,y) \approx \left(I_0 e^{-i\mu_0 x} + b_0 e^{i\mu_0 x} \right) \varphi_0(y) \tag{30}$$

$$\hat{\mathbb{L}}(x,y) \approx \left(I_0 e^{-i\mu_0 x} + \bar{b}_0 e^{i\mu_{m0} x} \right) \varphi_0(y) \tag{31}$$

where $b_0 = R_0 - T_0$ and $\bar{b}_0 = R_0 + T_0$ with R_0 and T_0 is the same as in Equation (16). The equation system presented in Appendix A can be solved numerically to determine $a_n, b_n, \bar{a}_n,$ and $\bar{b}_n$. Then, the reflection, transmission, and dissipation coefficients can be calculated along: $C_r = \left|(b_0 + \bar{b}_0)/2I_0\right|$, $C_t = \left|(b_0 - \bar{b}_0)/2I_0\right|$, and $C_e = 1 - C_r - C_t$, respectively.

To understand the effect of oblique incidence angle for different design parameters on the moored submerged flexible porous plate in the presence of a floating flexible plate, various results on the C_r, C_t, and C_e, as well as the submerged porous plate displacements, are analysed. From now on, all numerical results are performed by taking into account the same length, $2L$, for the floating and submerged plates; $\rho = 1025\text{kgm}^{-3}$; $g = 9.8\text{ms}^{-1}$; mooring stiffness, $q_f = q_s = 10^2\text{Nm}^{-1}$; Young's modulus, $E_1 = 0.47 \times 10^9\text{Nm}^2$ and $E_2 = 0.47 \times 10^7\text{Nm}^2$; compressive force on the floating plate, $N_1 = 0.5(E_1 I_1 \rho g)^{1/2}$; the submerged porous plate, $N_2 = 0.2(E_2 I_2 \rho g)^{1/2}$; $d/h = 0.25$; $L/h = 2.5$; $\sigma = 1.0 + 0.5i$; and plate thickness, $a_1 = a_2 = 0.1$m, if not otherwise specified.

MATLAB R2016b (MATLAB 9.1, source: *mathworks.com/trademarks*), 64-bit (win64) was used to perform calculations in a very quick manner. All numerical computations of the analytical expressions were performed on a desktop machine with Intel ® core i7–7700 CPU with a4.20 GHz processor and 16 GB of RAM, 3601 Mhz, 4 Core(s), and 8 Intel Processor(s). The data was written onto an SSD disk and, on average, each case took roughly 8–10 min to complete. Further, using the present solutions, MATLAB codes were developed to simulate the C_r, C_t, and C_e as well as the plate displacements.

3. Numerical Results and Discussions

It should be noted that to avoid repetition, the results analysis of the C_r, C_t, and C_e. for different design parameters versus non-dimensional wavelengths are deferred here (see [34]). Here, the new contribution is the analysis of the effect of oblique incidence angle on the reflection, transmission, and dissipation coefficients, and in addition, the structural displacements are presented.

Recently, the convergence of the C_r and C_e of a similar problem in two-dimensions was studied in [34] for different mooring stiffness and compressive force. Here, the convergence of the C_r and C_t of the series solution is checked for different oblique incidence angles with $d/h = 0.6$ and wave period T = 5 sec. Table 1 demonstrates the values of C_r and C_t converged to N $\geq$ 6 , and hence for computational accuracy, N $= 6$ is confined to compute C_r, C_t, and C_e.

Table 1. Convergence analysis.

Parameter	N	C_r	C_t
0^o	2	0.776671	0.122774
	3	0.776668	0.122773
	6	0.776669	0.122774
30^o	2	0.782145	0.137840
	3	0.775545	0.125941
	6	0.775542	0.125940
45^o	2	0.785870	0.139198
	3	0.774964	0.129311
	6	0.774961	0.129310
75^o	2	0.801884	0.140470
	3	0.779231	0.135731
	6	0.779228	0.135730

In Figure 2, the comparison of deflection amplitude (m) of the floating flexible plate between the present analytical against experimental datasets (see [30], Figure 8a) and the numerical FEM-BEM results (see [30], Figure 9c) versus non-dimensional wavenumber, $\beta_o L$, are plotted. The trends of the deflection amplitude are well captured and for smaller values of wavenumber, the data points are well in agreement between the two models. However, some data points are not matched well with the analytical results for higher wavenumbers.

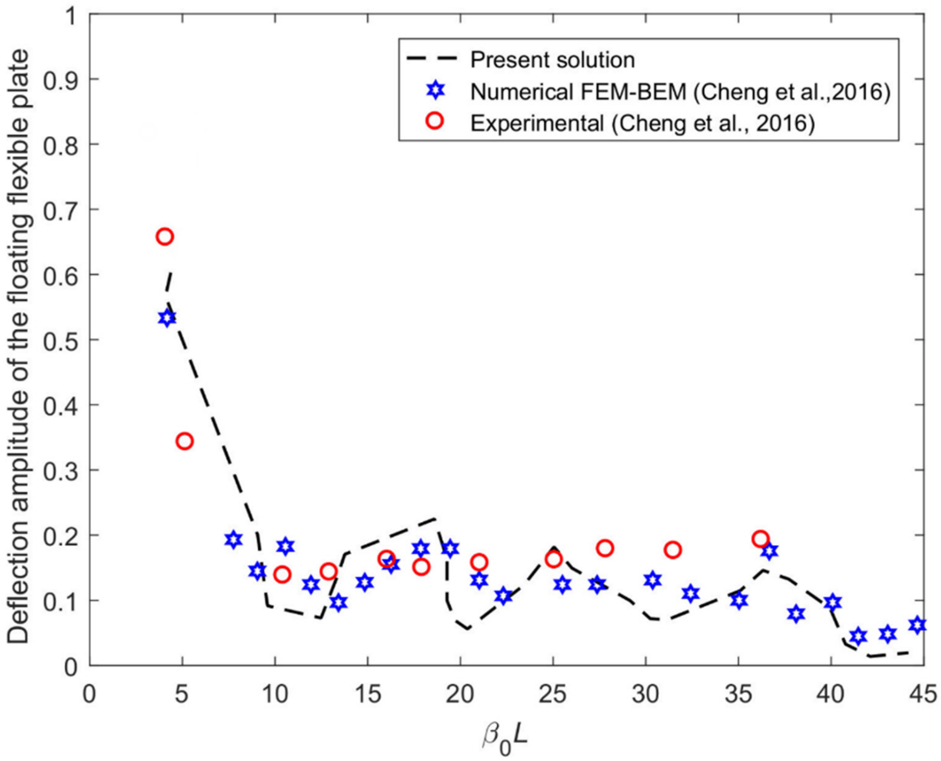

Figure 2. Comparison of the deflection amplitude with experimental datasets and FEM-BEM results for $\varepsilon = 0.5i$ and $d/h = 0.5$.

It should be mentioned that the interaction of a VLFS with a dual submerged horizontal porous plate is investigated in [30], where the ends of the VLFS were not moored. Here, the smaller values of mooring stiffness, $q_f = q_s = 10^2 \text{Nm}^{-1}$, and the critical value $N_2 = 0.5(E_2 I_2 \rho g)^{1/2}$ in Figure 2 is chosen to approach the free edge conditions and less compressive force. Therefore, the behaviour of the results between the model (see [30]) and the present one is deemed to be similar.

Comparison results showed that the trend of the deflection amplitude between the experimental and the numerical FEM-BEM (see [30]) with the present analytical results are all well captured. However, a very few experimental data points in the deflection amplitude are a little far from the model (see [30]) with a higher wavenumber. These deviations may be explained by the present solution associated with the two propagating wave modes along with compressive force in the flexible plates. Additionally, the effects of complex wavenumber and the compressive force considered in the present model can take part in the behaviour of the deflection pattern of the flexible plate, while these effects were not considered in [30]. Therefore, it is suspected that the present model reproduces a little lower deflection amplitude for higher non-dimensional wavenumber that the model (as in [30]) cannot reproduce.

3.1. Effect of Oblique Incidence Angles on the Reflection, Transmission, and Dissipation Coefficients

Figure 3 displays the effect of the C_r, C_e, and C_t versus oblique angle θ (deg.) for different mooring stiffness, q_f, of the floating flexible plate with $q_s = 10^2\mathrm{Nm}^{-1}$. The reflection coefficients, C_r, will be higher as the values of q_f increase, whilst the dissipation coefficients, C_e and C_t, decreases. However, for θ = 90°, it is seen that all incident waves neither reflected nor dissipated. This is due to the fact that both the floating and the submerged porous plates are considered to be of infinite length in the z-direction. Therefore, when the incident wave is perpendicular to the plate system, it propagates along the plate system in the z-axis direction only, and no there are no waves in the x-axis direction.

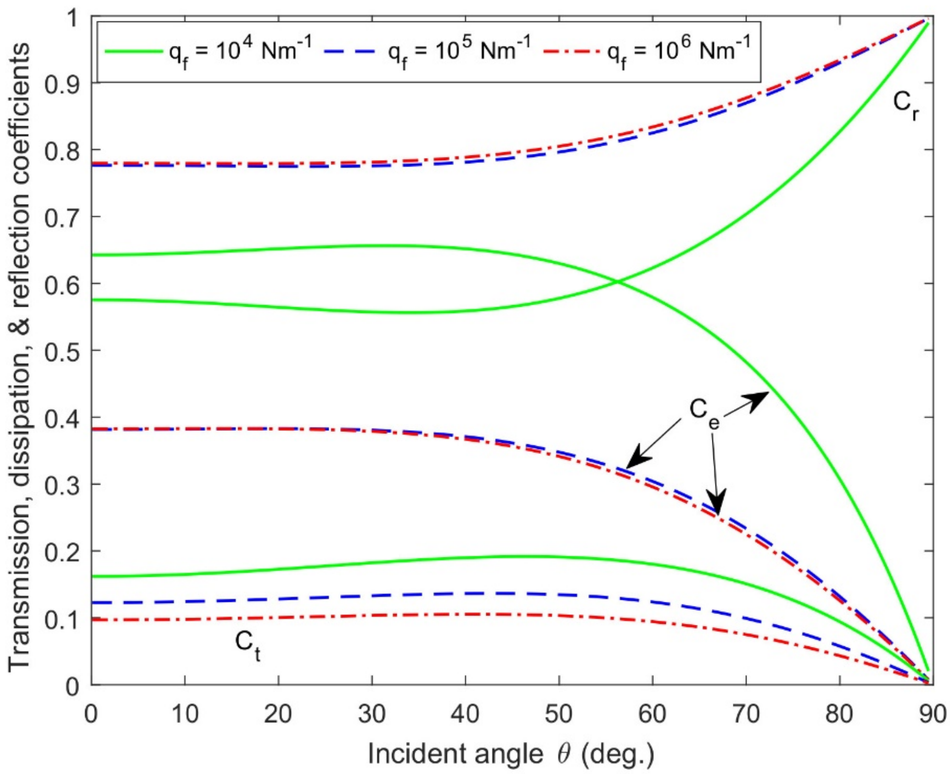

Figure 3. Effects of the C_r, C_e, and C_t against θ for different q_f with $q_s = 10^2\mathrm{Nm}^{-1}$.

Figure 4 shows the effect of N_1 on the reflection, transmission, and dissipation coefficients against θ with $N_2 = 0.2\sqrt{E_2 I_2 \rho g}$. As observed, the compressive force increases as C_r increases, while C_e and C_t become lower. This may be because, with an increase in the compressive force on the floating flexible plate, it becomes stiffer with a certain value of mooring stiffness in the submerged porous plate, which leads to higher reflection and smaller dissipation and transmission.

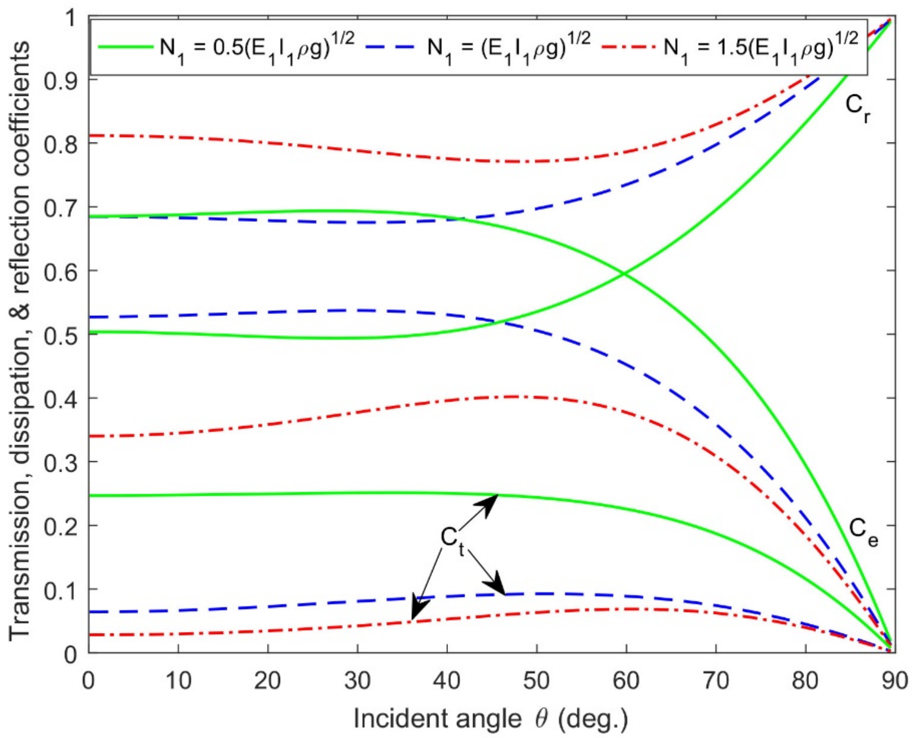

Figure 4. Effects of the C_r,C_t and C_e versus θ for different compressive forces, N_1.

In Figure 5, the comparison results of the C_r,C_t and C_e for various d/h versus angles θ are simulated. More importantly, the dissipation coefficient increases with an increase in the values of depth of submergence d/h, while the effect of transmission coefficient is negligible, as seen in Figure 5, which is due to a large portion of the wave energy being absorbed by the submerged porous plate.

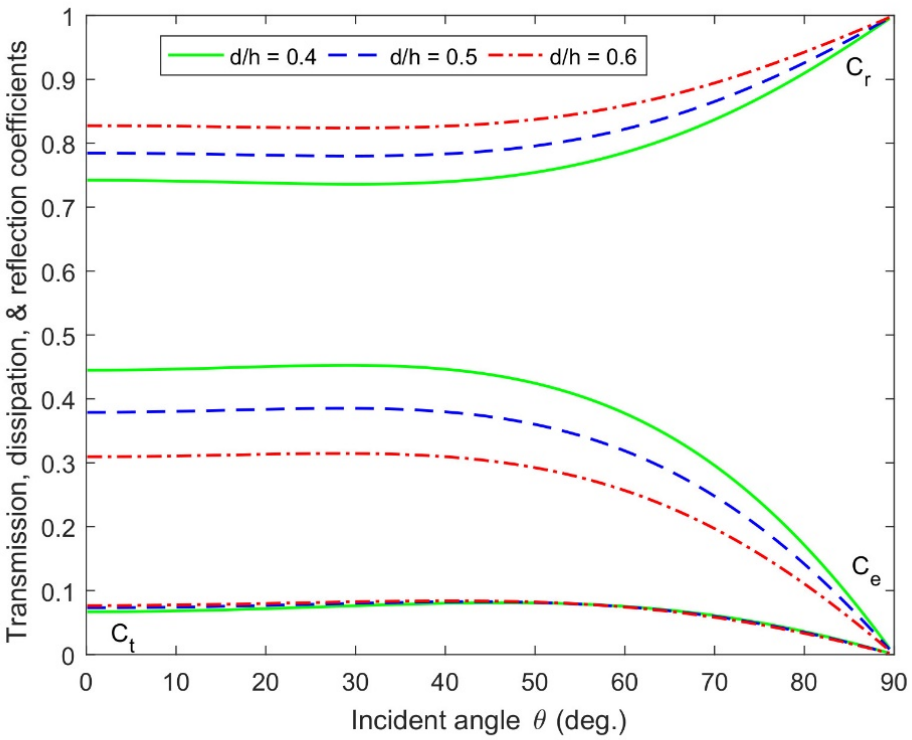

Figure 5. Effects of different d/h versus θ on C_r, C_t, and C_e.

Figure 6 gives the variations C_r,C_t, and C_e against θ on several structural lengths, L/h. It is observed that as the plate length increases, the C_r becomes lower and wave energy absorption over the submerged structure increases. This is due to the sizeableness of the flexibility and the pores in the plate.

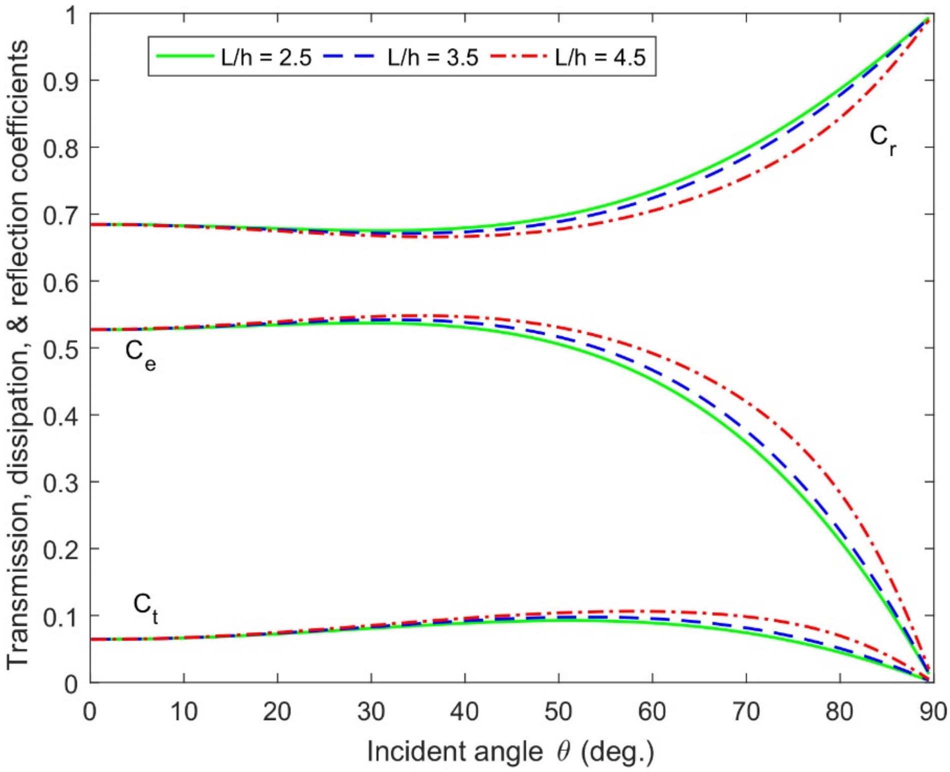

Figure 6. Effects of L/h on the C_r, C_t, and C_e versus θ with $\sigma = 1.0 + 0.5i$.

Figure 7 demonstrates the effect of the porous effect parameter on the reflection and dissipation coefficients C_r and C_e versus θ. It is observed that as the values of the porous parameter in the submerged flexible plate increase, the reflection coefficients, C_r, decreases, while the dissipation coefficients increase only for $\theta > 30^o$. However, for smaller angles,$\theta < 30^o$, the trend of C_e is reversed to that of $\theta > 30^o$, which is due to the change of phase of waves when the resistance force coefficient and inertial force coefficient of the porous-effect parameter are different.

It may be noted that, in Figures 3–6, the trend of the C_r,C_t, and C_e is significantly dependent on the value of mooring stiffness, compressive force, submergence depth, and plate length. For small wave angles ($\theta < 55^\circ$), the reflection coefficient becomes higher for higher mooring stiffness, submergence depth, and compressive force, while the C_t and C_e follow the reverse pattern. However, for $\theta = 90^\circ$, all incident waves neither reflected nor dissipated.

3.2. Structural Displacements via Hydroelastic Analysis

Figure 8 depicts the displacements, $w_2(\mathrm{m})$, of the moored submerged flexible porous plate for various oblique incidence angles: θ for $\sigma = 0.5i$ versus $\beta_0 h$ and plate length $L(\mathrm{m})$. From Figure 8a–d, it can be seen that, for higher oblique incidence angle, θ, the displacement of the submerged porous plate decreases, and only a single peak occurs at the edges of the plate.

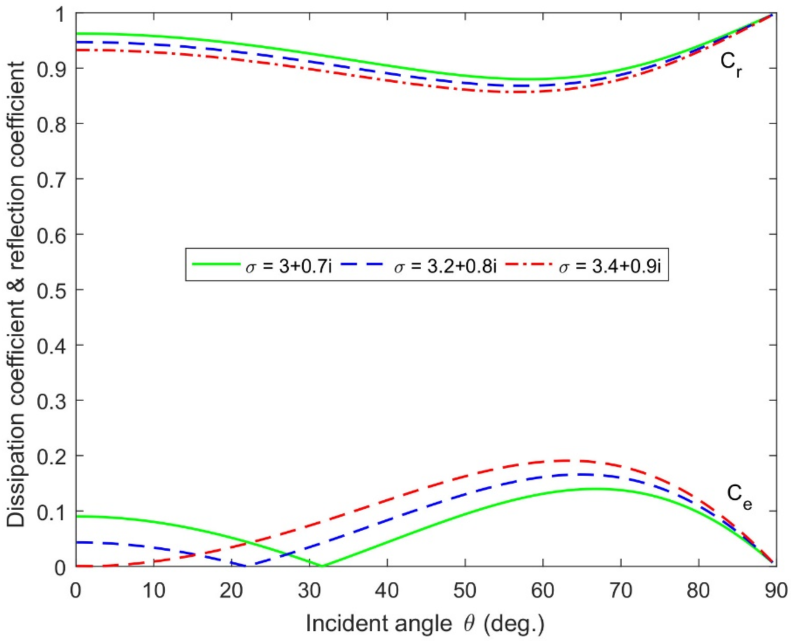

Figure 7. Effects of σ on the C_r and C_e versus θ with $d/h = 0.4$.

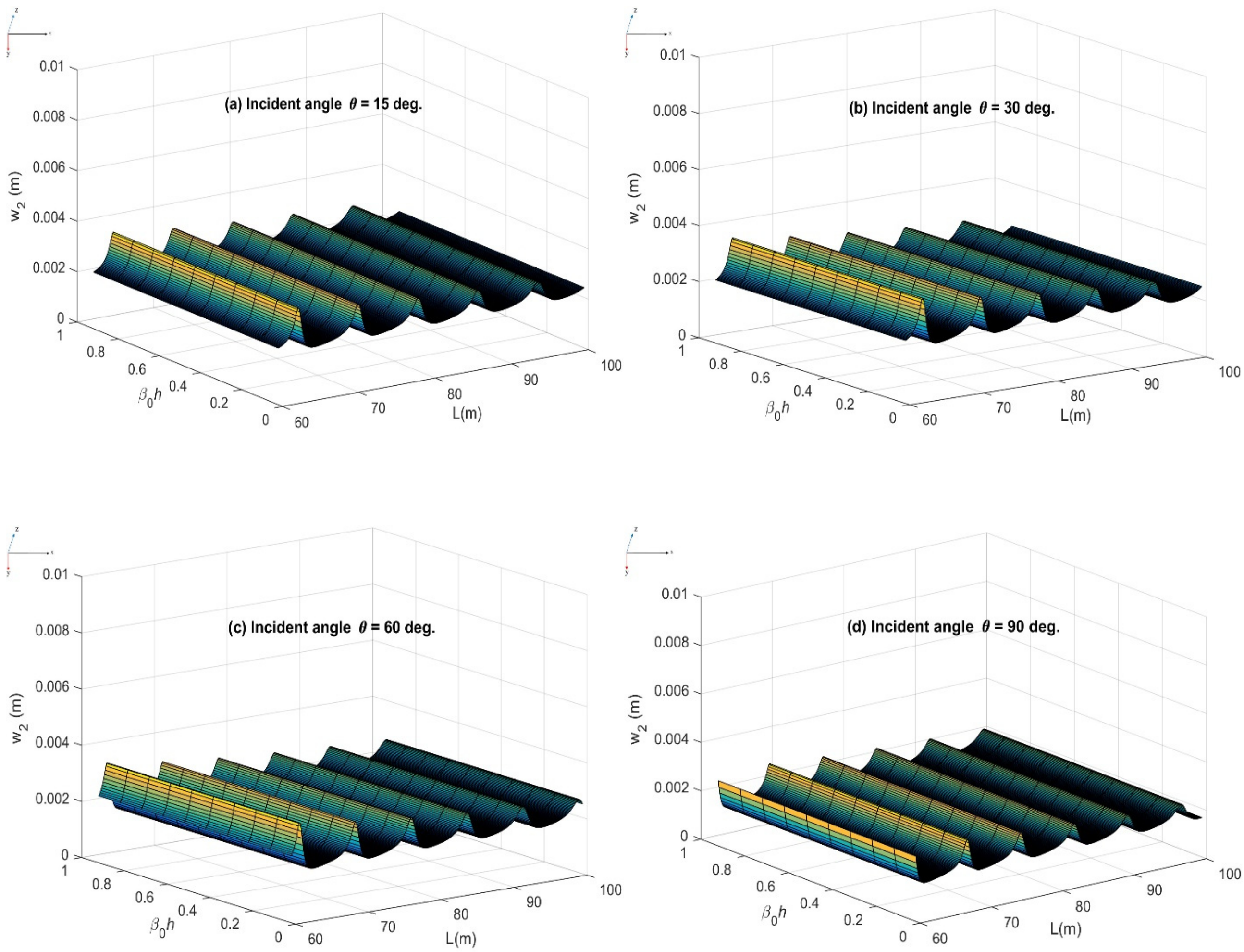

Figure 8. Displacement $w_2(\mathrm{m})$ with a floating flexible plate for different θ with $\sigma = 0.5i$ versus $\beta_0 h$ and $L(\mathrm{m})$.

Figure 9 demonstrates the displacements, $w_2(\mathrm{m})$, for different submergence depths with an incident angle versus non-dimensional wavenumber and plate length. From Figure 9a–d, it can be observed that, for higher submergence depth, the displacement amplitude of the submerged flexible plate becomes lower. This is due to less interaction with the floating plate and absorption of wave energy over the submerged porous plate.

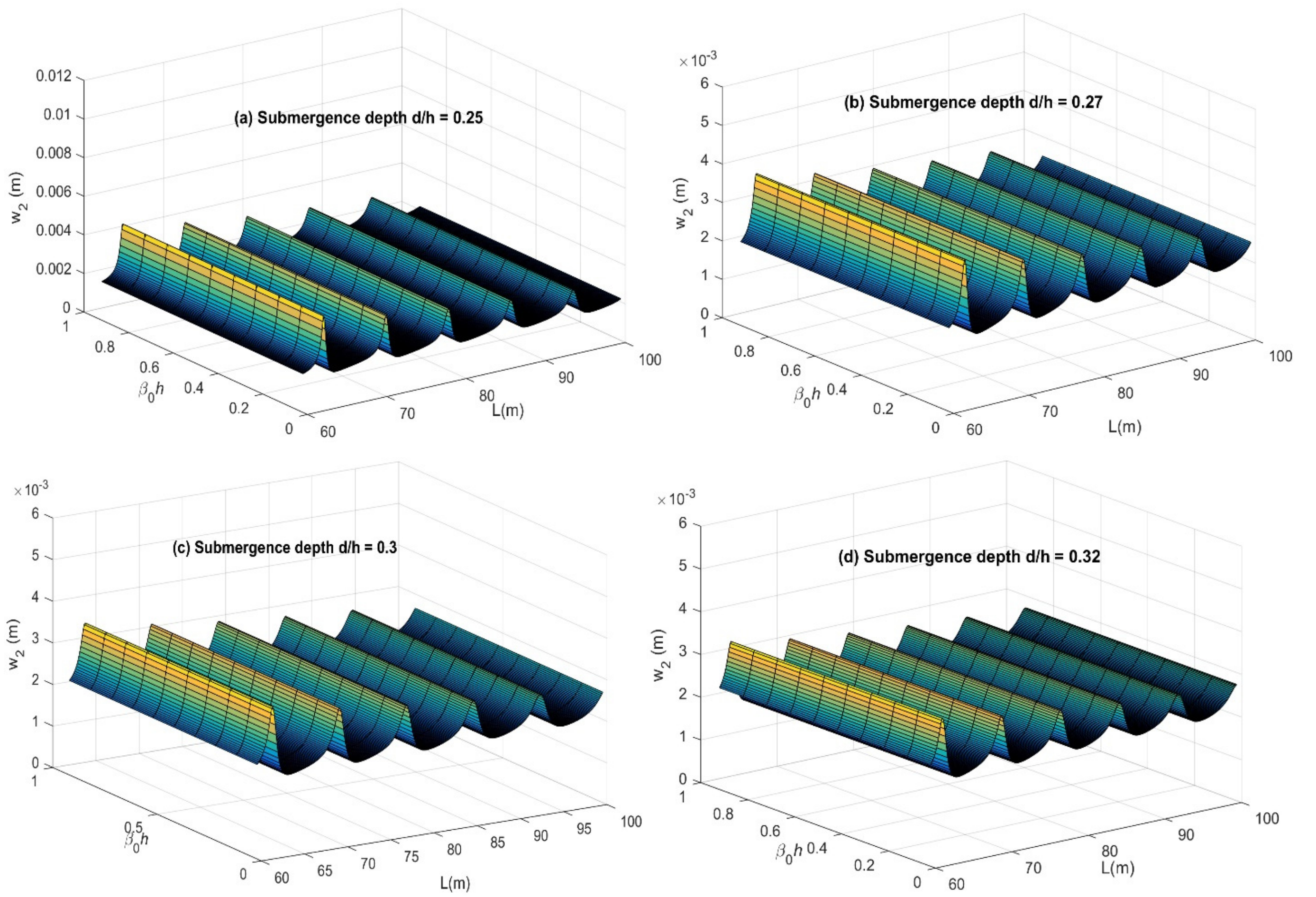

Figure 9. Submerged porous plate displacement with a floating flexible plate for various d/h with $\sigma = 0.5i$ and $\theta = 60$ (deg .).

Figure 10 simulates the displacements, $w_2(\mathrm{m})$, for various compressive forces, N_1, with $\sigma = 0.5i$ and $\theta = 60$ (deg .) versus non-dimensional wavenumber, $\beta_0 h$, and plate length, $L(\mathrm{m})$. In Figure 10a–d, for higher values of N_1, the deflections become smaller, which is due to the increased wave energy reflected as a result of less wave energy being absorbed by the submerged porous plate, which leads to lower deflection. Although the number of crests is the same in each case (a–d), the displacement amplitudes decrease as the values of compressive force become higher.

Figure 11 displays the submerged porous plate displacements for different mooring stiffness: (a) $q_s = 10^1\mathrm{Nm}^{-1}$, (b) $q_s = 10^2\mathrm{Nm}^{-1}$, (c) $q_s = 10^3\mathrm{Nm}^{-1}$, and (d) $q_s = 10^5\mathrm{Nm}^{-1}$ with $d/h = 0.25$. In Figure 11a–d, it can be clearly seen that the plate displacement decreases with an increase in the values of mooring stiffness. This is due to the fact that, as the stiffness of the mooring line increases, the flexibility of the plate becomes harder as a result of the decrease in the displacements of the flexible plate.

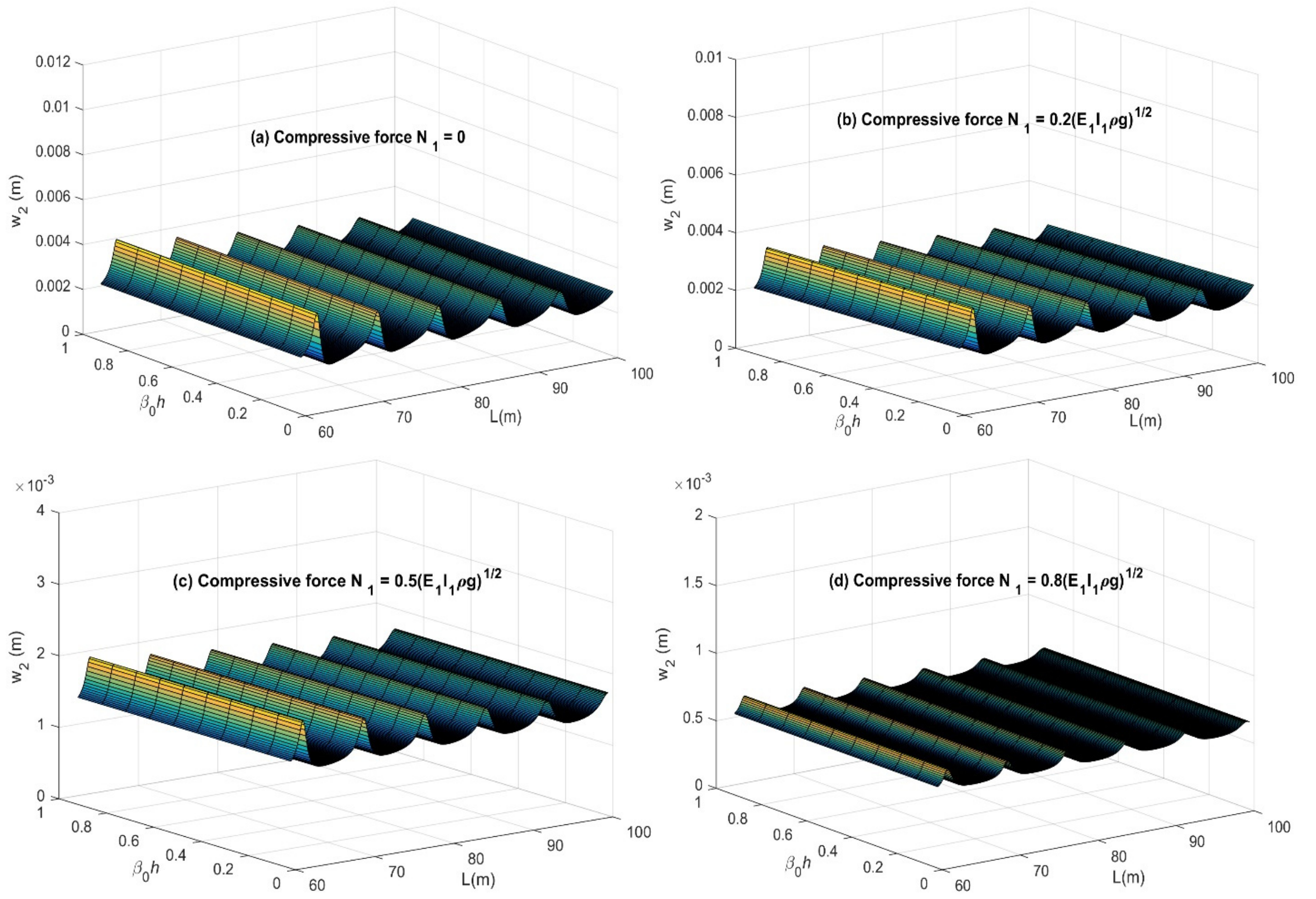

Figure 10. Porous plate displacement with floating flexible plate for different compressive forces with $\theta = 60$ (deg.) versus $\beta_0 h$ and $L(\mathrm{m})$.

It should be noted that there is only one single peak in each Figure (Figures 8–11) in the deflections being observed, which is due to the phase change of the incident and reflected waves, leading to constructive/destructive interference of the waves at the edge of the structure.

In the next section, the free oscillation hydroelastic waves in a wave tank of floating flexible plate in the presence of a submerged porous plate will be analysed in a specific case in two wave modes. In the case of surface wave interaction with a floating flexible plate in the presence of a horizontal flexible porous plate, two types of wave mode exist due to the interaction of waves with the floating plate and submerged flexible porous plate. One corresponds to the floating flexural mode (FFM) and another one corresponds to the submerged flexural mode (SFM). Further, the waves in the FFM are generated due to the presence of the floating flexible plate and the waves in SFM are generated because of the submerged flexible porous plate.

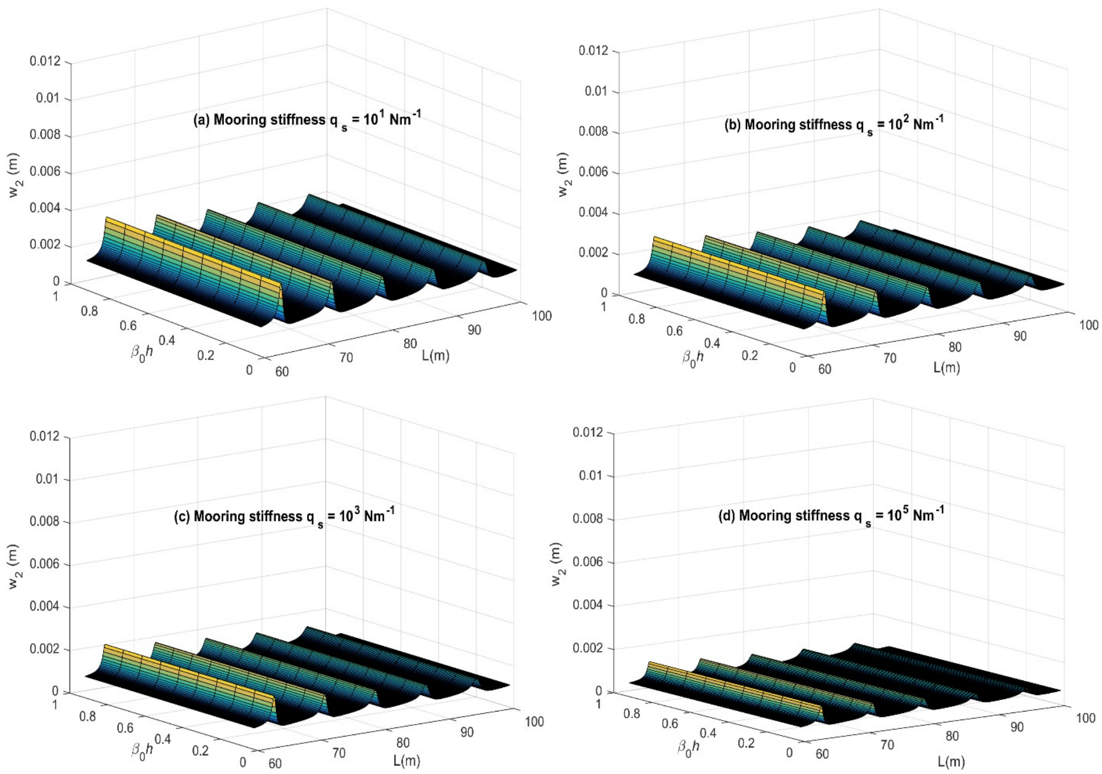

Figure 11. Influence of the mooring stiffnesses on the submerged flexible porous plate displacement for $\theta = 60^{\mathrm{o}}$ and $\sigma = 0.5i$.

4. Effect of Oblique Incidence Angle on the Hydroelastic Waves in a Wave Tank in FFM and SFM

The role of different design parameters on the hydroelastic waves in FFM and SFM in a two-dimensional closed wave tank was inspected in [34]. Here, the effects of oblique incidence angle on the phase and group velocities, dispersion curves, and period of oscillations in FFM and SFM are investigated.

Consider a basin bounded by vertical planes, $x = 0, l$, and a horizontal flexible plate floating at the free surface with a porous plate submerged below the floating plate; a detailed sketch of the arrangements is shown in Figure 12. Further, the basin length of $l(m)$ and $\gamma = \beta_0 \sin\theta$ present the z-component of the wavenumber, β_0, related to the plane progressive waves in the open water region, with an incidence angle of θ. It is assumed that the fluid characteristics and structural response is the same as discussed in Section 2.

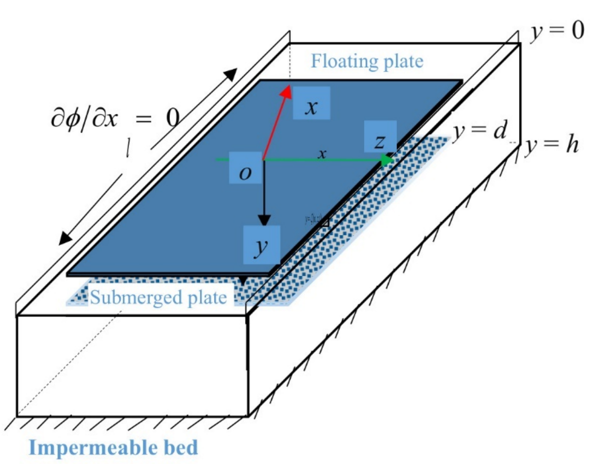

Figure 12. Graphical definition of the wave basin.

The velocity potential, $\phi(x,y)$, associated with the free motion can be expressed by satisfying Equations (1) and (3), boundary conditions (4)–(6) with $0 < x < l$, and $(\partial\phi/\partial x)|_{x=0,l} = 0$ as:

$$\Phi(x,y;t) = \sum_{n=1}^{\infty}\left\{\sum_{s=0}^{I}\mathcal{A}_n\mathcal{L}_{qn}(x,y)e^{i\omega_n^+ t} + \sum_{s=II}^{III}\mathcal{B}_n\mathcal{L}_{qn}(x,y)e^{i\omega_n^- t}\right\} \tag{32}$$

where the +ve sign corresponds to waves in FFM and the −ve sign corresponds to waves in the SFM. The waves in the FFM are generated due to the presence of the floating flexible plate, and the waves in SFM are generated by the presence of the submerged flexible porous plate. The values of ω^+ and ω^- are the frequencies of the waves in the FFM and SFM, respectively. Further, $\mathcal{L}_{sn}(x,y) = \cos(n\pi x/l)f_{sn}(\alpha_{sn},y)$, $f_{sn}(\alpha_{sn},y)$, and $s = 0,..,III$ are the same as in Equation (19), with $\alpha_{sn} = \left\{(n\pi/l)^2 + \gamma^2\right\}^{1/2}$, which satisfies the dispersion relation:

$$\tau = \frac{\alpha_{sn}(\kappa_1\alpha_{sn}^4 - \varepsilon_1\alpha_{sn}^2 + 1)}{\Lambda_n}, \tag{33}$$

where

$$\Lambda_n = \frac{\tau(1+\tanh\alpha_{qn}d\tanh\alpha_{qn}H) - \vartheta(\alpha_{qn})\left\{i\sigma(1+\tanh\alpha_{qn}d\tanh\alpha_{qn}H) + \tanh\alpha_{qn}H\right\}}{\tau(\tanh\alpha_{qn}d + \tanh\alpha_{qn}H) - \vartheta(\alpha_{qn})\left\{i\sigma(\tanh\alpha_{qn}d + \tanh\alpha_{qn}H) + \tanh\alpha_{qn}d\tanh\alpha_{qn}H\right\}} \tag{34}$$

with $\vartheta(\alpha_{qn}) = \alpha_{qn}(\kappa_2\alpha_{qn}^4 - \varepsilon_2\alpha_{qn}^2)$. The expression for Λ_n contains a ω^2 term, thus solving Equation (32) for ω^2 in terms of basin length and angle of incidence as $\alpha_{qn} = \left\{(n\pi/l)^2 + \gamma^2\right\}^{1/2}$. In the case of deep water, the dispersion relation (32) yields:

$$\omega_n^{2+} = g\alpha_{qn}(\kappa_1\alpha_{qn}^4 - \varepsilon_1\alpha_{qn}^2 + 1) \text{ and } \omega_n^{2-} = \frac{g\alpha_{qn}(\kappa_2\alpha_{qn}^4 - \varepsilon_2\alpha_{qn}^2)(1+2i\sigma)}{2} \tag{35}$$

Where the + and − signs correspond to the waves in FFM and SFM, respectively. From Equation (34), the phase velocities, v_n^{p+} in FFM and v_n^{p-} in SFM, are found to be:

$$v_n^{p+} = \sqrt{\frac{g(\kappa_1\alpha_{qn}^4 - \varepsilon_1\alpha_{qn}^2 + 1)}{\alpha_{qn}}} \text{ and } v_n^{p-} = \sqrt{\frac{g(\kappa_2\alpha_{qn}^4 - \varepsilon_2\alpha_{qn}^2)(1+2i\sigma)}{2\alpha_{qn}}} \tag{36}$$

Further, the group velocities, v_n^{g+} in FFM and v_n^{g-} in SFM, are obtained as:

$$v_n^{g+} = \frac{(5\kappa_1\alpha_{qn}^4 - 3\varepsilon_1\alpha_{qn}^2 + 1)\sqrt{g}}{2\sqrt{\alpha_{qn}(\kappa_1\alpha_{qn}^4 - \varepsilon_1\alpha_{qn}^2 + 1)}} \text{ and } v_n^{g-} = \frac{(5\kappa_2\alpha_{qn}^4 - 3\varepsilon_2\alpha_{qn}^2)\sqrt{g(1+2i\sigma)}}{2\left\{2\alpha_{qn}(\kappa_2\alpha_{qn}^4 - \varepsilon_2\alpha_{qn}^2)\right\}^{1/2}} \tag{37}$$

Finally, the period of hydroelastic wave oscillations, T_n^+, of the floating flexible plate in FFM and T_n^- of the submerged flexible porous plate in SFM are derived as:

$$\begin{aligned} T_n^+ &= \sqrt{\tfrac{4\pi}{g(n/a)(\kappa_1\alpha_{qn}^4 - \varepsilon_1\alpha_{qn}^2 + 1)}} \text{and} \\ T_n^- &= \sqrt{\tfrac{8}{g(n/a)^2\alpha_{qn}(\kappa_2\alpha_{qn}^2 - \varepsilon_2)(1+2i\sigma)}}. \end{aligned} \tag{38}$$

In the numerical results, the significant contributions to the effect of oblique incidence angle on the v_n^{p+}, v_n^{p-}, v_n^{g+}, v_n^{g-}, ω_n^{2+}, ω_n^{2-}, T_n^+, and T_n^- in FFM and SFM are analysed by comparing their results propagating in FFM and SFM.

The numerical results are computed by considering water density=$\rho = 1025$ kg/m^3, $d/h = 0.25$, gravitational constant, $g = 9.8$ ms^{-1}, $E_1I_1 = 0.47\times10^3$Nm^2, $E_2I_2 = 0.47\times10^2$Nm^2,

$N_1 = 1.2\sqrt{E_1 I_1 \rho g}$, $N_2 = (1/2)\sqrt{E_2 I_2 \rho g}$, $\sigma = 1.0 + i$, and $n = 1$ (n = 1 is considered for the sake of simplicity), if not otherwise specified).

Figure 13 compares the results of v_n^{p+} and v_n^{p-} for different values of oblique incidence angle, θ, versus l(m) are plotted. The phase velocity, v_n^{p-} , moves faster than those of v_n^{p+} for a shorter basin with different values of θ. However, in longer wave basins with lower values of θ, the phase velocity, v_n^{p-}, moves slower than those of v_n^{p+} due to the presence of compressive force and porosity in the submerged plate, which yields to the strong absorption of wave energy by the porous plate. On the other hand, at the edges of the basin, the variation of the effect of θ becomes significant in both the cases of v_n^{p-} and v_n^{p+}.

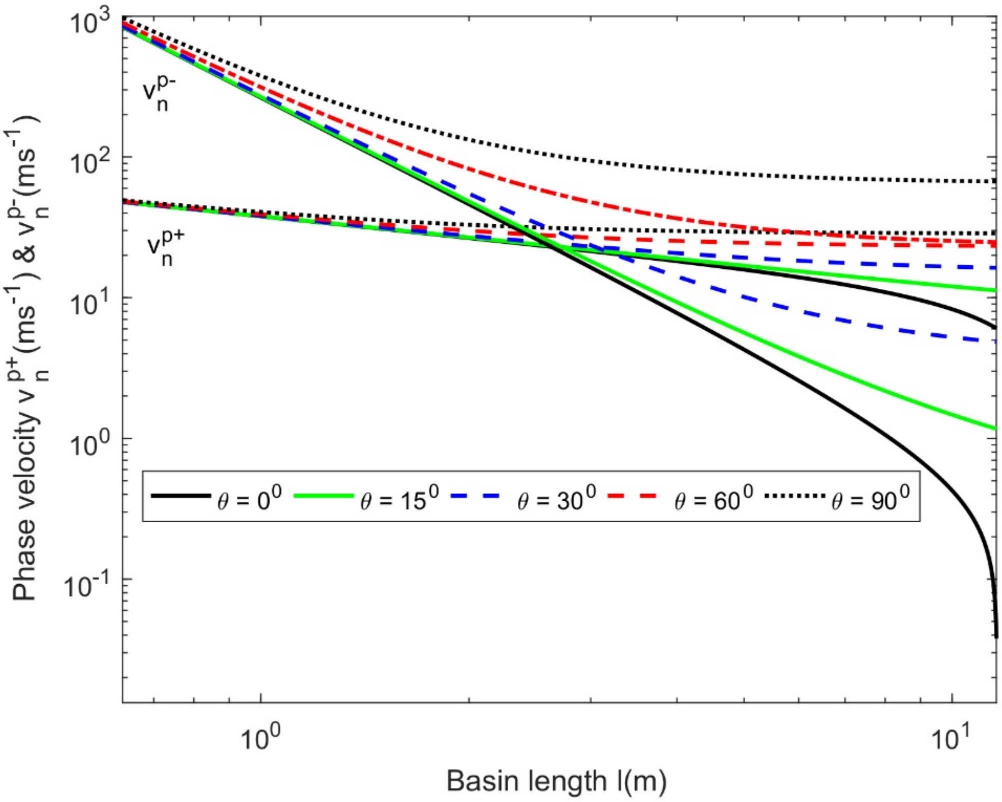

Figure 13. Effects of oblique angle, θ, on the phase velocity, v_n^{p+} and v_n^{p-} versus l(m).

Figure 14 compares the group velocity, v_n^{g+} and v_n^{g-}, for different θ against l(m). Figure 14 reveals that v_n^{g-} in SFM passes faster than those of v_n^{g+} in FFM for almost all higher values of θ. However, in a longer wave basin with lower values of θ, the group velocity, v_n^{g-}, in SFM moves slower than that of v_n^{g+} in FFM, for reasons similar to those in Figure 13. Further, it can be seen that the variations of v_n^{g+} in FFM for different values of oblique angle, θ, have no significant effect compared to v_n^{g-} in SFM. This can be attributed to the fact that the wave energy is dissipated by the submerged flexible porous plate, while less incident wave transmits, which leads to more impact to v_n^{g-} in SFM.

Figure 15 compares ω_n^+ in FFM and ω_n^- in SFM for different angles, θ, against l(m). It can be seen that, for higher values of the angle, θ, both ω_n^+ and ω_n^- increase. Further, the values of ω_n^+ are lower than those in SFM, which is due to the presence of porosity in the submerged flexible plate that absorbs wave energy. Further, it is also observed that, for a longer basin, the effect of oblique angle, θ, on the wave dispersion is significant while, for a shorter basin, the effect of θ is negligible.

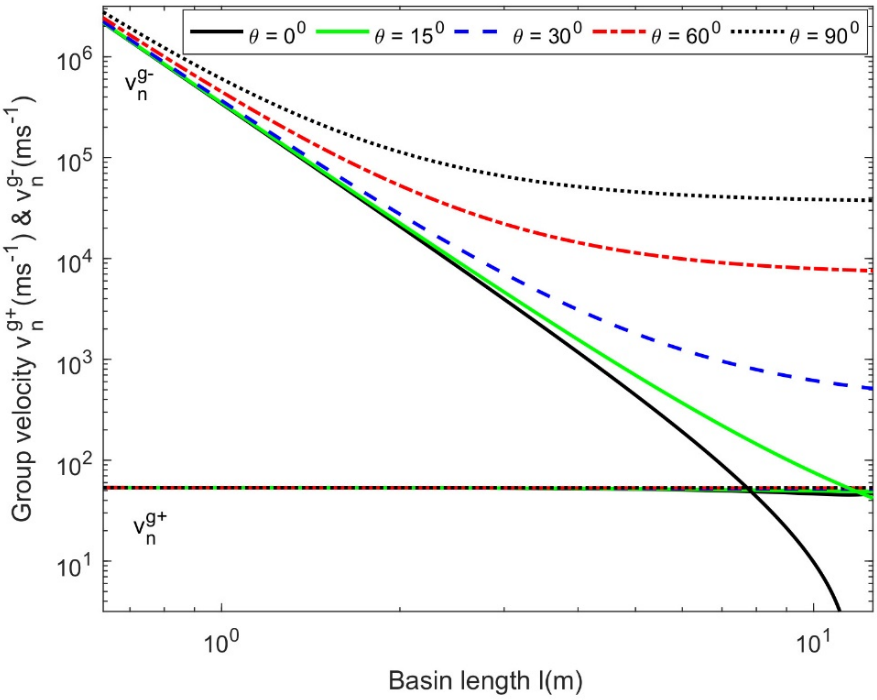

Figure 14. Effects of oblique incidence angle, θ, on v_n^{g+} and v_n^{g-} versus l(m).

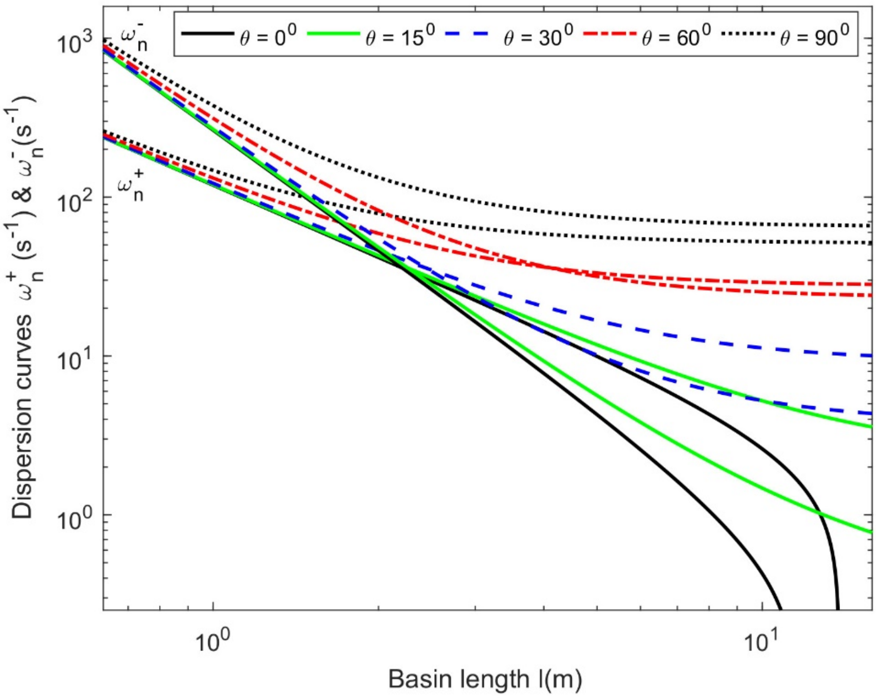

Figure 15. Effects of different oblique angles, θ, on ω_n^+ and ω_n^- against l(m).

In Figure 16, the period of oscillations, T_n^+ and T_n^-, decreases with an increase in the values of θ. This is due to the fact that, as the incident angle changes, the direction and types of the oscillation also change with their mode shapes, which results in a lower period of oscillation. However, the effect of θ is significant for a longer basin, and the vibration of the floating plate becomes less, possibly due to the wave energy absorbed by the porous plate.

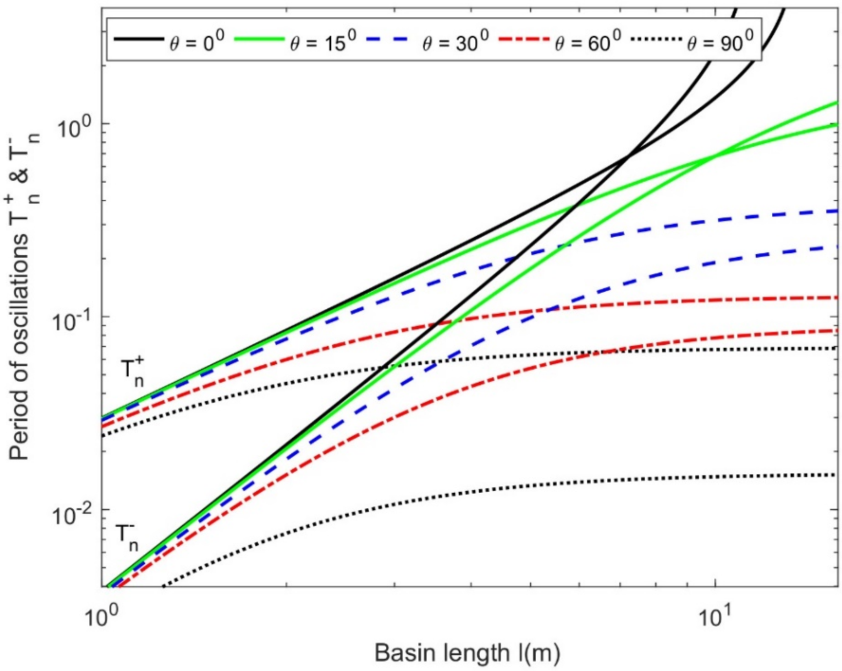

Figure 16. Comparison between T_n^+ and T_n^- versus l(m) for different θ.

Figure 17 shows the effect of the period of oscillation, T_n^-, on the increasing values of the porous-effect parameter versus basin length, $l(m)$, for different angles of incidence,θ. It can be seen that the period of oscillations, T_n^-, decreases with increasing values of θ. In the case of $\theta = 0^0$, the observation is similar to that obtained in [34]. However, the period of oscillation experienced peaks for zero incidence angle at around 10–15 m, which may be due to phase change of incident and reflected waves, leading to constructive/destructive interference of the waves in SFM. The decreasing rate of oscillation is much faster for increasing θ, and as the basin length increases, the period of oscillation reaches a smooth trend. One of the reasons for this may be the increasing rate of energy dissipation along the porous plate.

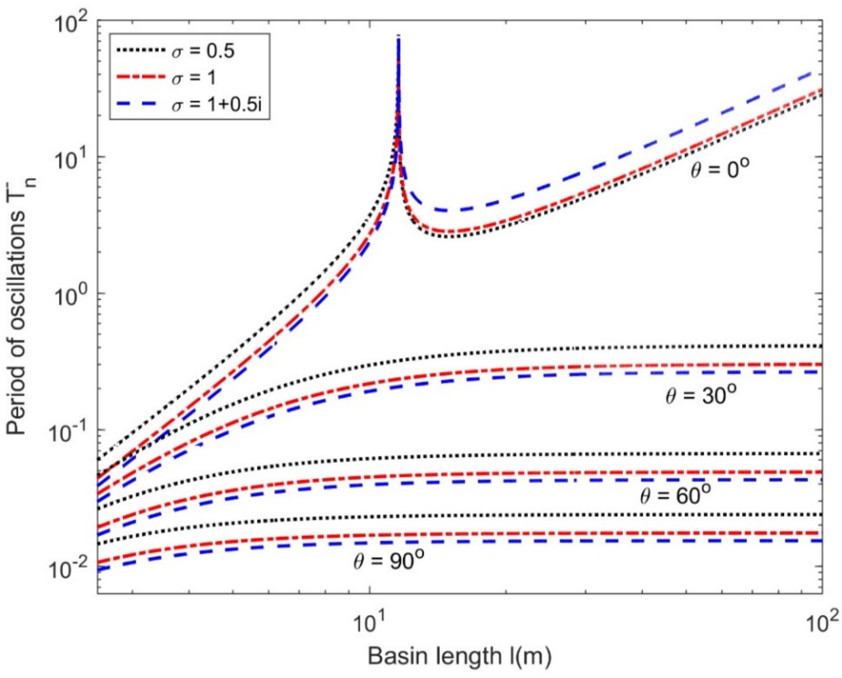

Figure 17. Effect of porous-effect parameter on T_n^- for different θ.

Figure 18 shows the effect of the first six modes, n, in the horizontal direction, on the period of oscillation, T_n^+, of the floating flexible plate with incidence angle $\theta = 30^0$ versus basin length $l(\mathrm{m})$. It is observed that the variations of the period of oscillations continue to decrease with an increase in basin length. This indicates that the modes of oscillation have an effect at the edges of the plate for a certain value of the incident angle, which changes the shape of the floating plate.

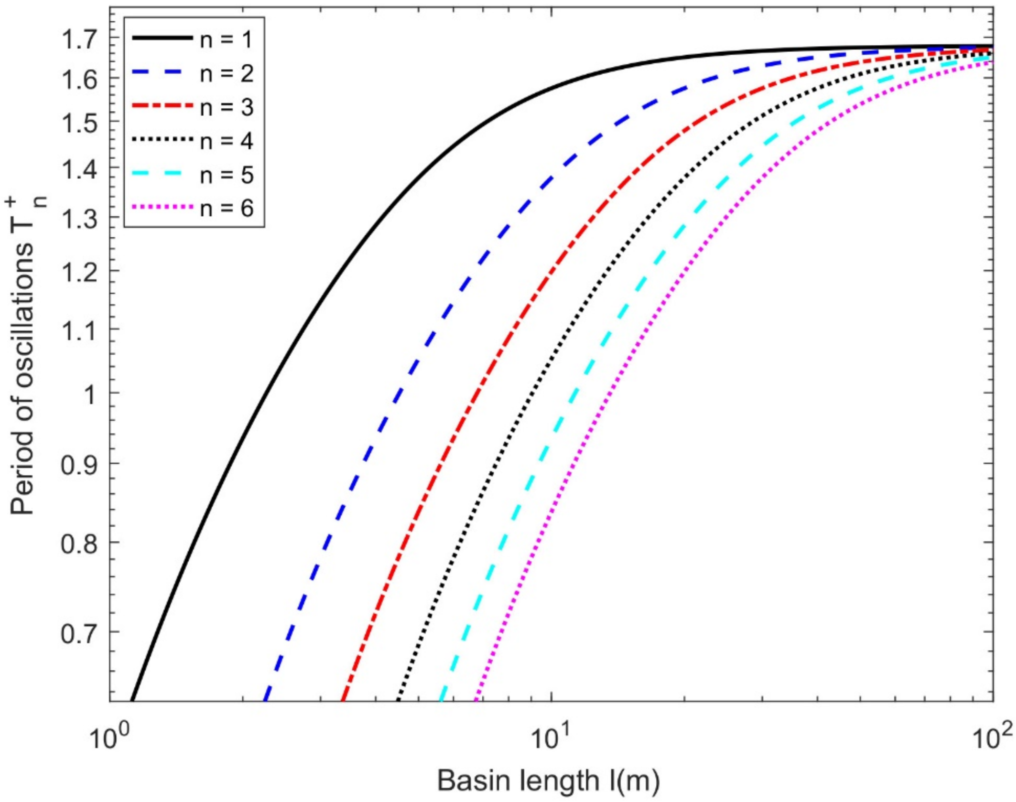

Figure 18. Effect of modes on the period of oscillation, T_n^+, of floating flexible plate with $\theta = 30^0$.

5. Conclusions

In this paper, a new contribution complementing [34] addresses the influence of oblique incidence angle based on the reduced wave equation. The hydroelastic analysis of a moored floating and a submerged flexible porous plate is investigated by studying the effect of the incident angle for different design parameters. Further, the free oscillation of hydroelastic waves in a wave basin is performed in specific cases. From the analysis, it has been observed that:

1. The convergence of the obtained solution is verified for different oblique incidence angles, and $N = 6$ is confined for computational accuracy.
2. It is found that the obtained results are supported by the published experimental and numerical FEM-BEM results.
3. For small oblique incidence angles ($\theta < 55°$), C_r increase for higher values of mooring stiffness and the compressive force of the floating plate with all parameters except porous-effect parameter associated with submerged porous plate, while C_t and C_e follow the reverse pattern. However, for $\theta = 90°$, the incident wave is normal to the floating and submerged flexible porous plates; it travels along with the plate in the z-direction, while the reflection C_r decreases and C_e increases for higher values of porosity.
4. The displacement results showed that, for compressive force and submergence depth, the amplitude of the plate displacement at the edges continues increasing as the incident angle increases, occurring a higher number of crests on the plate surface. On

the other hand, it is observed that the submerged porous plate deformation decreases with an increase in mooring stiffness.

5. In a closed wave basin, for the higher angle of incidence, the period of oscillations of hydroelastic waves over FFM and SFM decreases, while the $\omega_n^{\pm}$, $v_n^{p\pm}$, and $v_n^{g\pm}$ increase. Further, v_n^{p-} and v_n^{g-} move faster than that of v_n^{p+} and v_n^{g+}, having a significant effect of oblique incidence angle in a longer wave basin. The analysis of the results will be useful in the laboratory testing and design of a wave tank.
6. The present study indicated that the appropriate choice of oblique incidence angle, mooring stiffness, compressive force, and submergence depth will be useful to design a flexible plate system for an effective breakwater and the reduction of the hydroelastic response of floating flexible structures.
7. The limitations of the present study are that the relevant boundary conditions must be linear and of higher-order, maybe 3rd or 5th order, and the structural boundaries must be a constant of the co-ordinates; hence, the solution must be a series of solutions. Therefore, the present approach can be used for rectangular and circular-shaped flexible/porous plate and membrane type structures.
8. Further, the model formulation and calculation allow analysis of the hydrodynamic loads (horizontal and vertical) on the structure and the axial forces on the mooring lines.

Author Contributions: Conceptualization, S.C.M. and C.G.S.; methodology, S.C.M.; writing—original manuscript, S.C.M. and C.G.S. All authors have read and agreed to the published version of the manuscript.

Funding: This work contributes to the project HYDROELASTWEB—Hydroelastic behaviour of horizontal flexible floating structures for applications to Floating Breakwaters and Wave Energy Converters, which is funded by the Portuguese Foundation for Science and Technology (Fundação para a Ciência e a Tecnologia-FCT) under contract PTDC/ECI-EGC/31488/2017. The first author has been contracted as a researcher by the Portuguese Foundation for Science and Technology (Fundação para a Ciência e Tecnologia-FCT), through Scientific Employment Stimulus, Individual support under contract No. CEECIND/04879/2017. This work contributes to the Strategic Research Plan of the Centre for Marine Technology and Ocean Engineering (CENTEC), which is financed by the Portuguese Foundation for Science and Technology (Fundação para a Ciência e Tecnologia-FCT) under contract UIDB/UIDP/00134/2020.

Institutional Review Board Statement: Not applicable.

Informed Consent Statement: Not applicable.

Data Availability Statement: Not applicable.

Conflicts of Interest: The authors declare no conflict of interest.

Nomenclature

E_jI_j:	Flexural rigidities
N_j:	Compressive forces
w_1:	Floating plate deflection
w_2:	Submerged porous plate deflection
ω:	Angular frequency
σ:	Porous-effect parameter
ρ:	Density of water
Φ:	Velocity potential
ϕ_j:	Spatial velocity potentials
$\Psi_n^S(x,y)$:	Eigenfunction in plate covered region
$\Gamma_n(x,y)$:	Eigenfunction in open water region
mp_j:	Mass per unit length
a_j:	Thickness of the plates
g:	Gravitational constant
v:	Poisson's ratio

d:	Height between floating and submerged porous plate
h:	Water depth
H:	Depth between submerged porous plate and bottom
α:	Wavenumber in plate-covered region
γ:	z-component of the wavenumber associated with β_0 in the open water region
$\hat{\mathbb{L}}(x,y)$:	Split potential
$\mathbb{L}(x,y)$:	Split potential
$\varphi_n(y)$:	Normalized eigenfunction in the open water region
N:	Number of terms in the series
L:	Plate length
q_f:	Mooring stiffness of floating plate
q_s:	Mooring stiffness of the submerged porous plate
β_0:	Wavenumber of gravity wave dispersion relation
I_0:	Incident wave amplitude
C_r:	Reflection coefficient
C_t:	Transmission coefficient
C_e:	Dissipation coefficient
θ:	Incidence angle
BEM:	Boundary Element Method
FD:	Finite Water Depth
FFM:	Floating Flexural Mode
ID:	Infinite Water Depth
MEFEM:	Matched Eigenfunction Expansion Method
SFM:	Submerged Flexural Mode
VLFS:	Very Large Floating Structure

Appendix A. Equation System for Determining the Unknowns

A system of equations are obtained with $a_n, b_n, \overline{a}_n,$ and $\overline{b}_n$ in $\mathbb{L}(x,y)$ and $\hat{\mathbb{L}}(x,y)$ by utilizing the continuity condition at $x = L$ and orthogonal conditions (see [2]) as:

$$\sum_n a_n \Xi_{\nu n} - b_n \delta_{\nu n} + I_0 \delta_{\nu 0} = 0 \tag{A1}$$

$$\sum_n a_n \alpha_n \Xi_{\nu n} \coth \alpha_n L - i\mu_n \delta_{\nu n} b_n + i\mu_0 I_0 \delta_{\nu 0} = 0 \tag{A2}$$

$$\sum_n \overline{a}_n \Xi_{\nu n} - \overline{b}_n - I_0 \delta_{\nu 0} = 0 \tag{A3}$$

$$\sum_n \overline{a}_n \alpha_n \Xi_{\nu n} \tanh \alpha_n L - i\mu_n \overline{b}_n \delta_{\nu n} + i\mu_0 I_0 \delta_{\nu 0} = 0 \tag{A4}$$

where

$$n = 0, I, II, III, 1, 2, \ldots, N,\ \Xi_{\nu n} = \{\ell(\alpha_n, d) O_{\nu n} - S_{\nu n}\} / \left\{(\beta_\nu^2 - \alpha_n^2)\sqrt{\chi_\nu}\right\}$$

$$\begin{aligned} O_{\nu n} = {} & [\beta_\nu \{\tau \tanh \alpha_n d - \alpha_n(\kappa_1 \alpha_n^4 - \varepsilon_1 \alpha_n^2 + 1)\} \cos \alpha_n d - \alpha_n \coth \beta_\nu d] \sinh \beta_\nu d \\ & \times \{\tau \coth \alpha_n d + \alpha_n(\kappa_1 \alpha_n^4 - \varepsilon_1 \alpha_n^2 + 1)\} \sinh \alpha_n d \\ & + \alpha_n \{\alpha_n(\kappa_1 \alpha_n^4 - \varepsilon_1 \alpha_n^2 + 1) - \tau \coth \beta_\nu h\} \sinh \beta_\nu h, \end{aligned}$$

$$S_{\nu n} = (\beta_\nu \tanh \beta_\nu d - \alpha_n \tanh \alpha_n d) \cosh \alpha_n h \cosh \beta_\nu d,\ \ell(\alpha_n, d) = (\alpha_n \sinh \alpha_n d) / N_1'(\alpha_n, d)$$

Further, the boundary conditions (8, 9) and (10, 11) provide:

$$\sum_n a_n E_1 I_1 \alpha_n (\alpha_n^2 - \upsilon \gamma^2) \ell(\alpha_n, d) = 0 \tag{A5}$$

$$\sum_n a_n E_2 I_2 \alpha_n (\alpha_n^2 - \upsilon\gamma^2) \sinh\alpha_n d = 0 \quad \text{(A6)}$$

$$\sum_n \overline{a}_n \alpha_n^2 \ell(\alpha_n, d) [E_1 I_1 \left\{ \alpha_n^2 - (2 - \upsilon)\gamma^2 \right\} + N_1 - q_f] \tanh\alpha_n L = 0 \quad \text{(A7)}$$

$$\sum_n \overline{a}_n \alpha_n^2 [E_2 I_2 \left\{ \alpha_n^2 - (2 - \upsilon)\gamma^2 \right\} + N_2 - q_s] \tanh\alpha_n L \sinh\alpha_n d = 0 \quad \text{(A8)}$$

where $v = 0, 1, 2, \ldots, N$ and $m = 1, 2, 3, \ldots$. The system of Equations (A1)–(A8) can be solved numerically to determine $a_n, b_n, \overline{a}_n,$ and $\overline{b}_n$.

References

1. Loukogeorgaki, E.; Yagci, O.; Kabdasl, M.S. 3D Experimental investigation of the structural response and the effectiveness of a moored floating breakwater with flexibly connected modules. *Coast. Eng.* **2014**, *91*, 164–180. [CrossRef]
2. Mohapatra, S.C.; Guedes Soares, C. Hydroelastic response of a flexible submerged porous plate for wave energy absorption. *J. Mar. Sci. Eng.* **2020**, *8*, 698. [CrossRef]
3. Mohapatra, S.C.; Guedes Soares, C. Hydroelastic behaviour of a submerged horizontal flexible porous structure in three-dimensions. *J. Fluids Struct.* **2021**, *104*, 103319. [CrossRef]
4. Liu, Y.; Li, H. Hydrodynamic performance of a composite breakwater with an upper horizontal porous plate and a lower mound breakwater. *Ocean Syst. Eng.* **2013**, *3*, 55–70. [CrossRef]
5. Ohkusu, M.; Namba, Y. Hydroelastic analysis of a large floating structure. *J. Fluids Struct.* **2004**, *19*, 543–555. [CrossRef]
6. Watanabe, E.; Utsunomiya, T.; Wang, C.M. Hydroelastic analysis of pontoon-type VLFS: A literature survey. *Eng. Struct.* **2004**, *26*, 245–256. [CrossRef]
7. Anagnostopoulos, S.A. Dynamic response of offshore platforms to extreme waves including fluid-structure interaction. *Eng. Struct.* **1982**, *4*, 179–185. [CrossRef]
8. Korobkin, A.; Parau, E.I.; Broeck, J.M.V. The mathematical challenges and modelling of hydroelasticity. *Phil. Tran. R. Soc. A* **2011**, *369*, 2803–2812. [CrossRef]
9. Tsui, Y.-Y.; Huang, Y.-C.; Huang, C.-L.; Lin, S.-W. A finite-volume-based approach for dynamic fluid-structure interaction. *Numer. Heat Transf. B Fundam.* **2013**, *64*, 326–349. [CrossRef]
10. Xiang, T.; Istrati, D. Assessment of Extreme Wave Impact on Coastal Decks with Different Geometries via the Arbitrary Lagrangian-Eulerian Method. *J. Mar. Sci. Eng.* **2021**, *9*, 1342. [CrossRef]
11. Westphalen, J.; Greaves, D.M.; Raby, A.; Hu, Z.Z.; Causon, D.M.; Mingham, C.G.; Omidvar, P.; Stansby, P.K.; Rogers, B.D. Investigation of wave-structure interaction using state of the art CFD techniques. *Open J. Fluid Dyna.* **2014**, *4*, 18. [CrossRef]
12. Ren, B.; Jin, Z.; Gao, R.; Wang, Y.-X. SPH-DEM modeling of the hydraulic stability of 2D blocks on a slope. *J. Waterw. Port Coast. Ocean. Eng.* **2014**, *140*, 04014022. [CrossRef]
13. Hasanpour, A.; Istrati, D.; Buckle, I. Coupled SPH–FEM Modeling of Tsunami-Borne Large Debris Flow and Impact on Coastal Structures. *J. Mar. Sci. Eng.* **2021**, *9*, 1068.
14. Bispo, I.B.S.; Mohapatra, S.C.; Guedes Soares, C. Numerical analysis of a moored very large floating structure composed by a set of hinged plates. *Ocean Eng.* **2022**, *253*, 110785. [CrossRef]
15. Pham, D.C.; Wang, C.M.; Utsunomiya, T. Hydroelastic analysis of pontoon-type circular VLFS with an attached submerged plate. *Appl. Ocean Res.* **2008**, *30*, 287–296. [CrossRef]
16. Nguyen, H.P.; Dai, J.; Wang, C.M.; Ang, K.K.; Luong, V.H. Reducing hydroelastic responses of pontoon-type VLFS using vertical elastic mooring lines. *Mar. Struct.* **2018**, *59*, 251–270. [CrossRef]
17. Nguyen, H.P.; Wang, C.M. Finite element-Multi-domain boundary element method for hydroelastic analysis of large floating pontoons with perforated plates. *Ocean Eng.* **2022**, *246*, 110659. [CrossRef]
18. Karperaki, A.E.; Belibassakis, K.A. Hydroelastic analysis of very Large Floating Structures in variable bathymetry regions by multi-modal expansions and FEM. *J. Fluids Struct.* **2021**, *102*, 103236. [CrossRef]
19. Gerostathis, T.P.; Belibassakis, K.A.; Athanassoulis, G.A. 3D hydroelastic analysis of very large floating bodies over variable bathymetry regions. *J. Ocean Eng. Mar. Energy* **2016**, *2*, 159–175. [CrossRef]
20. Mohapatra, S.C.; Guedes Soares, C. Effect of mooring lines on the hydroelastic response of a floating flexible plate using the BIEM approach. *J. Mar. Sci. Eng.* **2021**, *9*, 941.
21. Feng, M.W.; Sun, Z.C.; Liang, S.X.; Liu, B.J. Hydroelastic response of VLFS with an attached submerged horizontal solid/porous plate under wave action. *China Ocean Eng.* **2020**, *34*, 451–462. [CrossRef]
22. Allsop, W.; Cuomo, G.; Tirindelli, M. New prediction method for wave-in-deck loads on exposed piers/jetties/bridges. *Coast. Eng.* **2006**, *5*, 4482–4493.
23. Azadbakht, M.; Yim, S.C. Effect of trapped air on wave forces on coastal bridge superstructures. *J. Ocean Eng. Mar. Energy* **2016**, *2*, 139–158. [CrossRef]
24. Istrati, D.; Buckle, I.; Lomonaco, P.; Yim, S. Deciphering the tsunami wave impact and associated connection forces in open-girder coastal bridges. *J. Mar. Sci. Eng.* **2018**, *6*, 148. [CrossRef]

25. Istrati, D.; Buckle, I. Role of trapped air on the tsunami-induced transient loads and response of coastal bridges. *Geosciences* **2019**, *9*, 191.
26. Xiang, T.; Istrati, D.; Yim, S.C.; Buckle, I.G.; Lomonaco, P. Tsunami Loads on a Representative Coastal Bridge Deck: Experimental Study and Validation of Design Equations. *J. Waterw. Port Coast. Ocean. Eng.* **2020**, *146*, 04020022. [CrossRef]
27. Cho, I.H.; Kim, M.H. Transmission of oblique incident waves by a submerged horizontal porous plate. *Ocean Eng.* **2013**, *61*, 56–65. [CrossRef]
28. Cho, I.H.; Koh, H.J.; Kim, J.R.; Kim, M.H. Wave scattering by dual submerged horizontal porous plates. *Ocean Eng.* **2013**, *73*, 149–158. [CrossRef]
29. Cheng, Y.; Ji, C.Y.; Zhai, G.; Oleg, G. Hydroelastic analysis of oblique irregular waves with a pontoon-type VLFS edged with dual inclined perforated plates. *Mar. Struct.* **2016**, *49*, 31–57. [CrossRef]
30. Cheng, Y.; Ji, C.Y.; Zhai, G.; Oleg, G. Dual inclined perforated anti-motion plates for mitigating hydroelastic response of a VLFS under wave action. *Ocean Eng.* **2016**, *121*, 572–591. [CrossRef]
31. Cheng, Y.; Zhai, G.; Ou, J.P. Time-domain numerical and experimental analysis of hydroelastic response of a very large floating structure edged with a pair of submerged horizontal plates. *Mar. Struct.* **2014**, *39*, 198–224. [CrossRef]
32. Mohapatra, S.C.; Guedes Soares, C. Effect of submerged horizontal flexible membrane on moored floating elastic plate. In *Maritime Technology and Engineering 3*; Soares, C.G., Santos, T.A., Eds.; Taylor & Francis Group: London, UK, 2016; pp. 1181–1188.
33. Mohapatra, S.C.; Guedes Soares, C. Interaction of ocean waves with floating and submerged horizontal flexible structures in three-dimensions. *Appl. Ocean Res.* **2019**, *83*, 136–154. [CrossRef]
34. Mohapatra, S.C.; Guedes Soares, C. Surface gravity wave interaction with a horizontal flexible floating plate and submerged flexible porous plate. *Ocean Eng.* **2021**, *237*, 109621. [CrossRef]
35. Yu, X. Diffraction of water waves by porous breakwaters. *J. Waterw. Port Coast. Ocean. Eng.* **1995**, *121*, 275–282. [CrossRef]